

OutLines: Modeling Spectral Lines from Winds, Bubbles, and Outflows

Sophia R. Flury ¹*

¹*Institute for Astronomy, University of Edinburgh, Royal Observatory, Edinburgh, EH9 3HJ, UK*

Accepted XXX. Received YYY; in original form ZZZ

ABSTRACT

Studies of kinematics and geometry of outflowing gas rely on modeling features in integrated spectra using empirical quantiles or fitting multiple Gaussian or Voigt profiles. Such methods can miss key underlying physics and even lead to spurious interpretations of observations. To address this problem, we present the public python code *OutLines*, which predicts spectral emission and absorption line profiles produced by winds, bubbles, and outflows. By design, *OutLines* is phenomenologically and scale agnostic to bridge the gap between observations and simulations across a broad swath of astrophysics. The *OutLines* code accounts for differences in velocity field, density profile, and outflow geometries, making *OutLines* versatile for a wide variety of astrophysical phenomena. We demonstrate the wide applicability of *OutLines* by using the code to model line profiles in an H II region knot, super star clusters, a starburst galaxy, and an AGN. In each of these contexts, we illustrate how *OutLines* can illuminate key underlying physics in ways that improve scientific understanding and address important open questions in astronomy, including the key mechanisms in the baryon cycle, the evolution of H II regions and galaxies, and even Lyman continuum escape. *OutLines* will be a critical resource as massively multiplexed spectroscopic surveys with facilities like WEAVE and 4MOST come online, providing the means to probe feedback with deeper, higher resolution spectroscopy for unprecedented large samples of objects.

Key words: ISM: jets and outflows – ISM: bubbles – ISM: kinematics and dynamics – galaxies: kinematics and dynamics

1 INTRODUCTION

Outflows, winds, and bubbles are ubiquitous astrophysical phenomena occurring on a dynamic range of spatial scales and in a variety of contexts, from young stellar objects (YSOs) to nebulae, active galactic nuclei (AGN), galaxies, and even galaxy clusters. This feedback has the capacity to shape many key astrophysical systems, from YSO winds affecting the formation of exoplanets (e.g., Suzuki & Inutsuka 2009; Manara et al. 2023) to massive stars redistributing the leftover material from their birth clouds (e.g., Dopita et al. 2005; Menon et al. 2024) to AGN and starbursts driving the baryon cycle of galaxies (e.g., Murray et al. 2005; Tumlinson et al. 2017). Many physical mechanisms can accelerate, or drive, winds and bubbles, from cosmic rays (e.g., Ipavich 1975) to hot expanding gas (e.g., Chevalier & Clegg 1985) to radiation pressure on dust (e.g., Poynting 1904; Lynden-Bell & Rees 1971) and ions (so-called line driving, e.g., Lucy & Solomon 1970), each with direct implications for how feedback shapes the surrounding environment (see, e.g., Veilleux et al. 2020; Thompson & Heckman 2024, and references therein). A common method of detecting and studying feedback is through broad, often asymmetric spectroscopic features (e.g., Castor 1970; Castor et al. 1975a; Noerdlinger & Rybicki 1974; Pelat & Alloin 1980; Pelat et al. 1981; Heckman et al. 1981; Chu & Kennicutt 1986), perhaps most famously with P Cygni wind lines in stellar atmospheres (e.g., Pauldrach et al. 1986; Lamers et al. 1987; Vink et al. 2001). Physically

motivated models for these line profiles is thus of critical importance to understanding how energetic phenomena shape their environment.

While the physics and formalism for spectroscopic features arising from winds, bubbles, and outflows is not new (e.g., Beals 1931; Sobolev 1960; Castor 1970; Castor et al. 1975a; Pauldrach et al. 1986; Lamers et al. 1987), their application is relatively sparse outside the phenomena of stellar atmospheres (e.g., Vink et al. 2001; Vink & Sander 2021; Sander et al. 2017; Puls et al. 2020). Instead, fitting multiple Gaussian or Voigt profiles to broad, asymmetric lines has become the standard (e.g., Pelat & Alloin 1980; Pelat et al. 1981) for a wide variety of objects, including H II regions (e.g., Bresolin et al. 2020; Yarovova et al. 2025), AGN (e.g., Liu et al. 2020), and galactic winds (e.g., Hogarth et al. 2020; Peng et al. 2023, 2025), despite early evidence that physics-based profiles are not only more appropriate but also demonstrably different in shape while still providing good descriptions of observations (e.g., Zheng et al. 1990; Tenorio-Tagle et al. 1996). Some studies have skirted the issue by adopting a more empirical approach using velocity quantiles (e.g., Heckman et al. 1981; Whittle 1985; Veilleux 1991) or by fitting the line profile wings with a log-linear (e.g., Komarova et al. 2021, 2025) or exponential (e.g., Rusakov et al. 2025) functions to characterize the steepness of the non-Gaussian flux distribution. The benefit of such methods is that they require no physical model while still providing insight into kinematics. However, bridging the gap between these approaches and the underlying physics is not always straightforward.

Some effort towards a physically motivated approach has emerged in recent years, including detailed treatment of radiation pressure and conservation effects (e.g., Krumholz et al. 2017), turbulent mix-

* E-mail: sflury@roe.ac.uk

ing layers (e.g., Binette et al. 2009), and relativistic accretion disk winds (e.g., Sim et al. 2008, 2010; Matzeu et al. 2022) along with more generalized models (e.g., Steidel et al. 2010; Prochaska et al. 2011; Martin et al. 2013; Scarlata & Panagia 2015; Chisholm et al. 2016; Luminari et al. 2018; Flury et al. 2023). Despite these exciting advancements, wide-spread adoption of these methods has stalled. A key to furthering the use of physically-motivated line profiles is versatile, well-documented, and user-friendly software tools which make such models readily accessible to the community to generate spectral line profiles linking observations to outflow physics without forward-modeling simulations.

In this paper, we present `OutLines`, a python-based code for generating model emission, absorption, and P Cygni line profiles arising from astrophysical winds, bubbles, and outflows on arbitrary spatial scales and independent of the phenomenon. The input geometry and wind physics can be readily customized, and functionality for modeling is provided. We outline the formalism and physics for radiative transfer, velocity fields, gas density profiles, and geometry in §2. Then, in §3 we present the implementation of these components in the `OutLines` code¹. We demonstrate the versatile applicability and scientific usefulness of `OutLines` in §4 by modeling broad spectral lines in an H II region knot, a super star cluster (SSC), a starbursting galaxy, and an active galactic nucleus (AGN), with profiles generated by `OutLines`. In the final case, we demonstrate that `OutLines` can successfully recover wind geometry through comparison with observations. Finally, we summarize `OutLines` and its potential for high scientific impact in §5, providing details of code setup and installation in Appendix B and worked examples in Appendices C and D.

2 PHYSICAL MODEL

Within the framework of the Sobolev approximation (Sobolev 1944, 1957, 1960), small scale Doppler motions of gas within clouds can be ignored in the context of the large-scale motion of the clouds themselves. The Sobolev approach has a long-standing precedent in the study of winds (e.g., Castor 1970; Noerdlinger & Rybicki 1974; Mihalas et al. 1975; Lamers et al. 1987), with successful application to galactic winds and outflows over the past 15 years (e.g., Steidel et al. 2010; Prochaska et al. 2011; Martin et al. 2013; Scarlata & Panagia 2015; Chisholm et al. 2016; Flury et al. 2023). Under this assumption, the key characteristics of winds, outflows, and bubbles which dictate the line profile are the velocity field, density profile, and geometry of the clouds (e.g., Zheng et al. 1990). Below, we elaborate how the observed projected velocity u in a spectral line, given by the longitudinal relativistic Doppler shift (Einstein 1905, also Sher 1968 their Eqn 4) such that

$$u = \frac{c}{v_\infty} \frac{(\lambda/\lambda_0)^2 - 1}{(\lambda/\lambda_0)^2 + 1} \quad (1)$$

for a line with rest wavelength λ_0 and normalized to the wind terminal velocity v_∞ and reducing to the classical Doppler shift $u = c(\lambda/\lambda_0 - 1)/v_\infty$ when $v_\infty \ll c$, relates to the intrinsic wind velocity w given by some radially-symmetric velocity field

$$w = \frac{v_{\text{wind}}[x, \beta]}{v_\infty} \quad (2)$$

with respect to some radial distance $x = r/R_0$ from the source of the outflow, with radius R_0 , and defined by some exponent β . In

¹ available at github.com/sflury/OutLines and via pip install.

addition to the velocity field, one must also know the radial gas density distribution, given by

$$n'[r] = n_0 n[x] \quad (3)$$

for a dimensionless profile n and maximum density n_0 , and the azimuthal geometry of the wind. With the velocity field w , density profile n , and outflow geometry in hand, radiative processes can translate outflows from the frame of the source to the spectral line in the frame of the observer.

2.1 Radiative Processes

Below, we outline the formalism for absorption and emission line profiles arising from astrophysical winds, with implicit assumptions about the velocity field $w[x]$, the radial gas distribution $n[x]$, and the gas geometry.

2.1.1 Line Absorption

In general, line absorption optical depth τ_λ at any particular wavelength λ in a feature is given by

$$\tau_\lambda = \frac{N}{v} f \lambda_0 \sigma_a \phi_\lambda \quad (4)$$

where v is the velocity scale of the line (b in the case of static interstellar medium (ISM) lines, v_∞ in the case of winds), N is the column density of the gas, f is the quantum mechanical oscillator strength, λ_0 is the rest wavelength of the electronic transition which absorbs incident light, $\sigma_a = 10^{-14.8427} \text{ cm}^2 \text{ s km}^{-1}$ is the classical absorption cross-section per unit wavelength per unit velocity, and ϕ_λ is the line profile evaluated at λ . Traditional treatment of the static interstellar medium (ISM) assumes a Voigt profile for ϕ_λ (most robustly calculated using the real part of the Faddeeva function, although approximations can also be used, e.g., Hjerting 1938; Tepper-García 2006) to account for kinetic and natural broadening.

Under the Sobolev approximation, instead one must evaluate the relative column density at each velocity w in the wind or bubble that is projected onto the line of sight velocity u . The optical depth profile for the outflow component given by the Sobolev approximation is thus

$$\phi_\lambda = K^{-1} \int n[x] \frac{dx[w]}{dw} d\Omega' \quad (5)$$

over some observed differential solid angle $d\Omega'$ given by the geometry (see Rybicki & Hummer 1983, their Equation 2.14) and where K is a normalization constant ensuring $\int_\lambda \phi_\lambda d\lambda = 1$ (Rybicki & Lightman 1979, their Equation 1.65). The differential term $\frac{dx}{dw}$ arises from integrating over all column densities associated with the observed velocity u (Castor 1970, their Equation 6, Chisholm et al. 2016, their Equation 4, assuming no stimulated emission). The corresponding integral limits are given by constraints from the geometry (§2.4). Following the equation of radiative transfer, one must sum up contributions of each velocity slice to the optical depth, not to the emergent flux, or else risk falling victim to Jensen's inequality ($\exp[-\int \tau] < \int \exp[-\tau]$) by over-estimating the column density and optical depth (e.g., Jennings et al. 2025).

The emergent flux, including a static component with a Voigt profile, is therefore given by

$$\frac{F_\lambda}{F_{\lambda 0}} = \exp[\tau_s \phi_{\lambda, \text{Voigt}} + \tau_o \phi_{\lambda, \text{out}}] \quad (6)$$

for intrinsic (backlight) flux density $F_{\lambda 0}$ and emergent flux density F_{λ} and where

$$\tau_s = f\lambda_0\sigma_a b^{-1}N_s \quad (7)$$

for static gas column density N_s , and

$$\tau_o = f\lambda_0\sigma_a v_{\infty}^{-1}N_o \quad (8)$$

for outflowing gas column density N_o .

2.1.2 Nebular Line Emission

For nebular emission lines, the emergent line flux density F_{λ} is simply the profile ϕ_{λ} scaled by the integrated line flux F such that

$$F_{\lambda} = F\phi_{\lambda} \quad (9)$$

for any given wavelength. “Static” gas undergoes Doppler broadening from thermal, orbital, and turbulent motion which produces the traditional Gaussian form of ϕ_{λ} . In the case of an outflow, we must first consider how the line emission depends on density and velocity. The line emission coefficient j_{λ} is typically defined as proportional to the density of the populated upper state producing the transition (Rybicki & Lightman 1979; Osterbrock & Ferland 2006). Since nebular lines emerge from upper electronic states populated by recombination or collisional excitation, $j \propto n[x(w)]^2$ (e.g., Osterbrock & Ferland 2006; Peimbert et al. 2017). Thus, we can simply express the line profile as

$$\phi_{\lambda} = K^{-1} \int n[x[w]]^2 d\Omega' \quad (10)$$

where K again is a normalization constant ensuring $\int_{\lambda} \phi_{\lambda} d\lambda = 1$ (see Flury et al. 2023). As with absorption, limits on the integral are given by the geometry in §2.4.

The emergent flux, including a static component with a Gaussian profile, is then given by

$$F_{\lambda} = F_s\phi_{\lambda,\text{Gauss}} + F_o\phi_{\lambda,\text{out}} \quad (11)$$

for nebular emission.

2.1.3 Resonant and Fluorescent Line Emission

Unlike nebular line emission, which depends on collisional and recombination processes, the upper state population of resonant and fluorescent lines depends primarily on the absorption of photons which are subsequently re-emitted in a random direction. Therefore, the line emission coefficient j_{λ} is proportional to ndx/dw , meaning that the line profile is determined using Equation 5 but with integral limits for line emission given by integrating over the entire volume (see §2.4). However, photons emitted in this fashion can be re-absorbed and subsequently re-emitted in an arbitrary direction, effectively a scattering process, which will alter the line profile. Resonant and fluorescent lines re-emit light which has previously been absorbed isotropically, meaning that the line flux is determined by the source function $S_{\lambda} = 1 - \exp[-\tau_{\lambda}]$ (see, e.g., Castor 1970, their §6, Rybicki & Hummer 1983, their §3) such that

$$\frac{F_{\lambda}}{F_{\lambda 0}} = \epsilon f_{\text{esc},\lambda} (1 - \exp[-\tau_{\lambda}]) \quad (12)$$

where τ_{λ} is given by line absorption in Equations 4 and 5 with integral limits consistent with line emission in Equation 10, ϵ is the filling factor to account for clumpiness because individual clouds do not sample every possible sightline even when they are isotropically

distributed, and $f_{\text{esc},\lambda}$ is the fraction of photons which escape radiative trapping at a given wavelength λ . The escape fraction of photons depends on the fraction $p_i = A_i/\sum A$ of photons which are produced by a transition i given by the transition rate A_i divided by the total radiative depopulation rate $\sum A$, where each i corresponds to a resonant (p_{res}) or fluorescent (p_{fluor}) channel. Following formalism from Castor (1970, their Equation A12, see also Rybicki & Hummer 1983, their Equation 3.19), the probability that a resonant photon can escape from radiative “trapping” through resonant scattering is given by the ratio of emission to absorption $(1 - \exp[-\tau_{\text{res},\lambda}])/\tau_{\text{res},\lambda}$. Trapped photons either scatter through emission and re-absorption in the resonant channel or re-emit in the fluorescent channel. After multiple scatterings, the resonant photons are increasingly trapped relative to the fluorescent photons, meaning that the escape fraction is

$$f_{\text{esc},\lambda}^{\text{res}} = p_{\text{res}} \frac{1 - \exp[-\tau_{\text{res},\lambda}]}{\tau_{\text{res},\lambda}} \left(1 - p_{\text{res}} \frac{1 - \exp[-\tau_{\text{res},\lambda}]}{\tau_{\text{res},\lambda}} \right)^{-1} \quad (13)$$

for resonant photons and

$$f_{\text{esc},\lambda}^{\text{fluor}} = p_{\text{fluor}} \left(1 - p_{\text{res}} \frac{1 - \exp[-\tau_{\text{res},\lambda}]}{\tau_{\text{res},\lambda}} \right)^{-1} \quad (14)$$

for fluorescent photons under the infinite scattering limit given by Scarlata & Panagia (2015, their Equations 20a,b).

2.2 Solutions to Wind Equations of Motion

Velocity profiles for winds can take on a variety of shapes arising from different treatments of the wind equations of motion (e.g., CAK theory Castor et al. 1975a; Lamers & Morton 1976; Abbott 1977; Barlow & Cohen 1977; Castor & Lamers 1979). The simple β law approximation

$$w[x] = (1 - x^{-1})^{\beta}, \quad \text{BetaCAK} \quad (15)$$

first appears in early treatment of Wolf-Rayet P Cygni lines for $\beta = 0.5$ (Equation 23 Castor 1970) and arises from a generalization of CAK theory solutions (see, e.g., Equation 47 of Castor et al. 1975a) without loss of physical insight (see, e.g., Barlow & Cohen 1977; Castor & Lamers 1979; Pauldrach et al. 1986). The CAK β law approximation is ubiquitous in the study of stellar winds (e.g., Vink et al. 2001; Vink & Sander 2021; Telford et al. 2024) and has even seen application to galactic outflows (e.g., Chisholm et al. 2016; Flury et al. 2023). Given its widespread adoption and underlying physical motivation, the CAK β law is our default and fiducial velocity field.

In addition to the β law approximation to CAK theory, OutLines includes two alternate solutions to the wind equations proposed in the literature. The first, from Steidel et al. (2010), assumes a power law approximation to the radial acceleration field to obtain

$$w[x] = (1 - x^{1-\beta})^{1/2}, \quad \text{AccPlaw} \quad (16)$$

where the normalization terms are implicit in w and x and $r_{\text{min}} = 1$. While those authors do not provide a corresponding physical model, their acceleration power law has a velocity field qualitatively similar to those of Ipavich (1975), which assumed cosmic ray driving, and Chevalier & Clegg (1985), which assumed constant momentum and energy deposition into a steady-state wind from a fluid in which it is entrained (see also, e.g., Owocki 2025), and formally akin to radiative acceleration of expanding clouds (see Equations 16-17 Mathews 1974). Note that the acceleration power law field with $\beta = 2$ is identical to that of the CAK β law when $\beta = 0.5$.

The second velocity field alternative, from various sources (e.g., [Faucher-Giguère & Quataert 2012](#)), constitutes a power law approximation to the radial velocity field such that

$$w[x] = A(x-1)^\beta, \quad \text{VelPlaw} \quad (17)$$

where the wind is assumed to accelerate from rest at R_0 and A scales the field. We set $A = 0.5$ to allow clouds to reach 50% terminal velocity in roughly the same range of radii as the CAK theory β law and generally overlap with the same region in w - x space as both the CAK β law and acceleration power law fields. Single-shell models of stellar wind bubbles can give rise to power law velocity fields from the shared time dependence of $r \propto t^{3/5}$ and $v \propto t^{-2/5}$ ($v \propto r^{-2/3}$, e.g., [Weaver et al. 1977](#); [Dyson 1977](#)). Building on this framework, [Faucher-Giguère & Quataert \(2012\)](#) arrive at a velocity power law solution assuming continuous production of “shells” by an AGN to produce a wind.

While the OutLines default assumes that gas is launched from rest, we have allowed for the possibility that the gas starts from some launch velocity v_0 , which we include as an optional free parameter. The velocity limits are accordingly updated so that the minimum velocity w_ℓ which contributes to an observed velocity $|u|$ is never below v_0/v_∞ . The velocity fields in [Table B3](#) and [Equations 15-17](#) are modified by a factor of $1 - v_0/v_\infty$ with the addition of a constant v_0/v_∞ such that the relative velocity not from rest w_{nfr} is

$$w_{\text{nfr}} = w[x|\beta] \left(1 - \frac{v_0}{v_\infty}\right) + \frac{v_0}{v_\infty} \quad (18)$$

(e.g., [Castor & Lamers 1979](#)). Emergent profiles are similar to those presented in [Tenorio-Tagle et al. \(1996\)](#), which included distributions of non-zero shell ages, and to those presented in [Scarlata & Panagia \(2015\)](#), which account for non-zero launch velocities. For visualization purposes, we assume in example profiles in [§2](#) that $v_0 = 0.1v_\infty$.

[Figure 1](#) depicts the different velocity fields for a range of β . From this comparison, as suggested by the formalism, the power law velocity field approaches v_∞ more rapidly than the power law acceleration field or the β -law approximation to CAK theory, reaching v_∞ at distances far closer to the launch radius. Moreover, the power law velocity field does not approach v_∞ asymptotically as do the other velocity fields, meaning that the stopping condition at v_∞ is imposed solely by integral limits rather than the formalism for the velocity field. We note that physical wind models almost always exhibit an acceleration which gradually decreases as the outflow asymptotically approaches some terminal velocity (e.g., [Castor et al. 1975a](#); [Barlow & Cohen 1977](#); [Chevalier & Clegg 1985](#); [Thompson et al. 2015](#); [Krumholz et al. 2017](#); [Ishibashi et al. 2018](#); [Quataert et al. 2022b](#)), indicating that the underlying wind physics strongly favors a CAK β law or acceleration power law field over a velocity power law field. While individual wind bubble models indicate a velocity power law field (e.g., [Weaver et al. 1977](#); [Dyson 1977](#)), in ensembles of shells, the distribution of shell ages will dominate the net velocity field (e.g., [Tenorio-Tagle et al. 1996](#)) and is likely determined by the physical driving mechanism (e.g., [Chu & Kennicutt 1994](#)), suggesting that the CAK theory or acceleration power law velocity fields provide a more physically appropriate description for wind scenarios. That being said, the velocity power law field prescription can be consistent with turbulent streaming including the classic Kolmogorov cascade, with the case of $\beta = 1$ indicative of Couette flow (e.g., [Binette et al. 2009](#)), although such scenarios may not capture the underlying driving mechanism.

We illustrate the effect of varying the velocity field for fixed β and the default OutLines geometry and density profiles in [Figure](#)

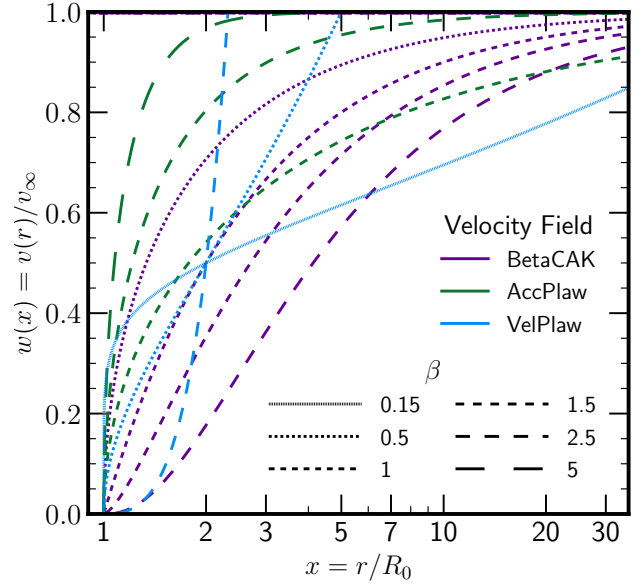


Figure 1. Radial velocity fields included in OutLines and given by [Equations 15-17](#). Acceleration from rest at the base R_0 of the wind ($x = 1$) proceeds until the wind reaches the terminal velocity v_∞ ($w[x] = 1$). Velocity fields include the [Pauldrach et al. \(1986\)](#) β law approximation to CAK theory ([Castor et al. 1975a](#)) (blue, [Equation 15](#)), the [Steidel et al. \(2010\)](#) power law acceleration (green, [Equation 16](#)), and the power law velocity field (purple, [Equation 17](#)). Dash length increases with increasing β .

2. As suggested by the velocity fields in [Figure 1](#), the acceleration power law causes $w \rightarrow 1$ more rapidly than the other two scenarios, resulting in more emergent flux at higher projected velocities and thus the most pronounced intermediate wings. The β CAK law field more rapidly populates moderate velocities than the velocity power law field, resulting in a slightly brighter core. However, the acceleration of the velocity power law field overtakes that of the β CAK at high velocities, producing more prominent broad wings in the former than the latter.

2.3 Radial Density Profiles

The gas / clouds within a wind likely vary with projected radial distance from the launching source due to a variety of factors, including conservation of cloud surface area (e.g., [Krumholz et al. 2017](#)), fountains (e.g., [Leroy et al. 2015](#)), or an isothermal mass-conserving gas (e.g., [Rupke et al. 2005b](#); [Prochaska et al. 2011](#)).

We adopt a smooth function to describe a continuous distribution of delta functions, with each delta function “pulse” representing an instantaneous burst or ejection of material with gas density n from the launch site and projected radially. For simplicity, n can be assumed to follow a power law such that

$$n[x] = x^{-\alpha}, \quad \text{PowerLaw} \quad (19)$$

a reasonable approximation for stellar and galactic winds (e.g., [Castor & Lamers 1979](#); [Chevalier & Clegg 1985](#), respectively) and a common choice in the literature (e.g., [Faucher-Giguère & Quataert 2012](#); [Scarlata & Panagia 2015](#); [Chisholm et al. 2016](#); [Flury et al. 2023](#); [Luminari et al. 2024](#)) arising from power law solutions to differential equations (as also the case for the velocity profile) and can be indicative of momentum or energy conservation ($\beta = (\alpha - 2)/2$ and $\beta = (\alpha - 2)/3$, respectively [Faucher-Giguère & Quataert 2012](#),

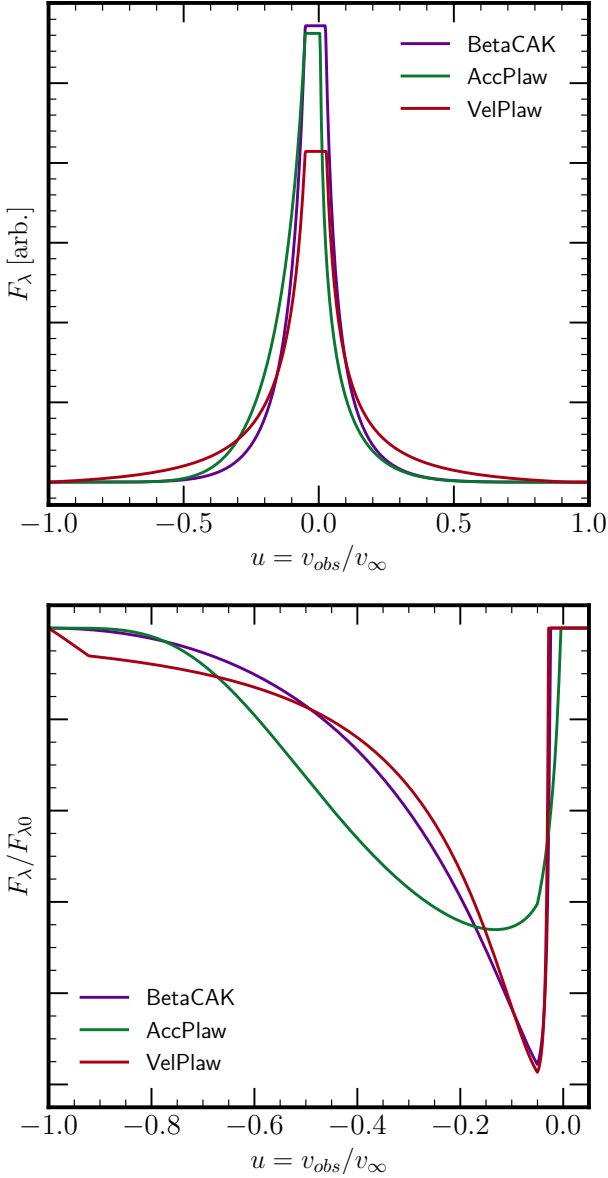


Figure 2. Nebular emission (*top*) and resonant absorption (*bottom*) line profiles for each of the velocity fields included in OutLines assuming $\beta = 1.5$ (CAK theory), $\beta = 1$ (velocity power law), and $\beta = 2$ (acceleration power law) for the OutLines defaults.

for the power law velocity field β). Perhaps intuitively, $\alpha = 2$ represents a mass-conserving scenario with density changing only as a r^{-2} projection effect. As an alternative, we can adopt an exponential profile where

$$n[x] = \exp[-\gamma(x-1)], \quad \text{Exponential} \quad (20)$$

which is also readily invoked from solutions to differential equations and may correspond to the relaxation or dissipation of wind material as it projects out from the launch point. For cases where a continuous flow may flatten or precipitously decline beyond some radius, we also implement a broken power law

$$n[x] = \begin{cases} x^{-a_1}, & x < x_1 \\ x_1^{a_2-a_1} x^{-a_2}, & x > x_1 \end{cases}, \quad \text{PowerLaw2} \quad (21)$$

with a break-point or “knee” at radius x_1 , inner slope a_1 and outer slope a_2 . Examples of a broken power law include the shock-driven outflow launched by the interaction of winds from massive stars in proximity to Sag A* ($a_1 < a_2$, drop off in density profile, e.g., Quataert 2004) and the relativistic outflow triggered by the waking/activating supermassive black hole in Swift J164449.3+57345 ($a_1 > a_2$, flattening in density profile, e.g., Berger et al. 2012).

For a variety of physical scenarios, including swept up shells and blast waves, we also allow in OutLines the possibility of pulse-like radial density profiles consistent with a shell or bubble with a scaled radius $x_1 = R_{\text{shell}}/R_0$ and characteristic width $\sigma_x = \sigma_r/R_0$, including a shell with gas in a normal distribution

$$n[x] = \left(2\pi\sigma_x^2\right)^{-1/2} \exp\left[-\frac{(x-x_1)^2}{2\sigma_x^2}\right], \quad \text{Normal}, \quad (22)$$

with a log normal distribution

$$n[x] = \left(2\pi(\log \sigma_x)^2\right)^{-1/2} \exp\left[-\frac{(\log x - \log x_1)^2}{2(\log \sigma_x)^2}\right], \quad \text{LogNormal}, \quad (23)$$

a fast-rise exponential decay (or FRED, Equation 24, see Norris et al. 2005) distribution

$$n[x] = \exp[2\mu] \exp\left[-\frac{\tau_1}{x + \mu - x_1} - \frac{x + \mu - x_1}{\tau_2}\right], \quad \text{FRED}, \quad (24)$$

$$\mu = \sqrt{\tau_1 \tau_2}$$

a logistic column density distribution

$$n[x] = \frac{k \exp[-k(x-x_0)]}{(1 + \exp[-k(x-x_0)])^2}, \quad \text{DLogistic}, \quad (25)$$

and a uniform distribution

$$n[x] = \begin{cases} \frac{1}{2\sigma_x}, & |x - x_1| < \sigma_x \\ 0, & \text{otherwise} \end{cases}, \quad \text{UniformShell}. \quad (26)$$

These pulse-like density profiles are consistent with simple single expanding shells or bubbles which are symmetric (normal or uniform), leading (FRED), or trailing (log normal) material with respect to the outward direction of the gas. We illustrate the continuous and pulse-like density profiles available in OutLines in Figure 3.

We show the effects of changing the density distribution for a fixed density (n_0), total column density (N), and velocity field (β , v_∞) in Figure 4 assuming a spherical geometry. The emission line profile wings for the shell or pulse-like density distributions are distinct from the continuous distributions; however, distinctions among the various subsets are less clear, likely owing to the geometric dilution of the density profile by integrating over the entire volume of the line-emitting gas. The effect of pulse profiles on the emission line profile is largely consistent with early fixed-velocity single expanding shell models for Wolf-Rayet features and stellar wind bubbles wherein no line core emerges (e.g., Beals 1931; Tenorio-Tagle et al. 1996). Such marked differences in radial gas distribution may explain the line profiles of ionized gas around pre- and post-SNe stellar populations as in the different clusters in the Sunburst Arc (e.g., Mainali et al. 2022).

The absorption line profiles are more distinct for each individual density profile, likely owing to the direct tracing of the line-of-sight gas distribution without any geometric dilution. Deviations from spherical geometry may affect this result, particularly in the case of a narrow bicone normal to the plane of the sky and aligned with the observer, which directly traces the density distribution in emission and absorption.

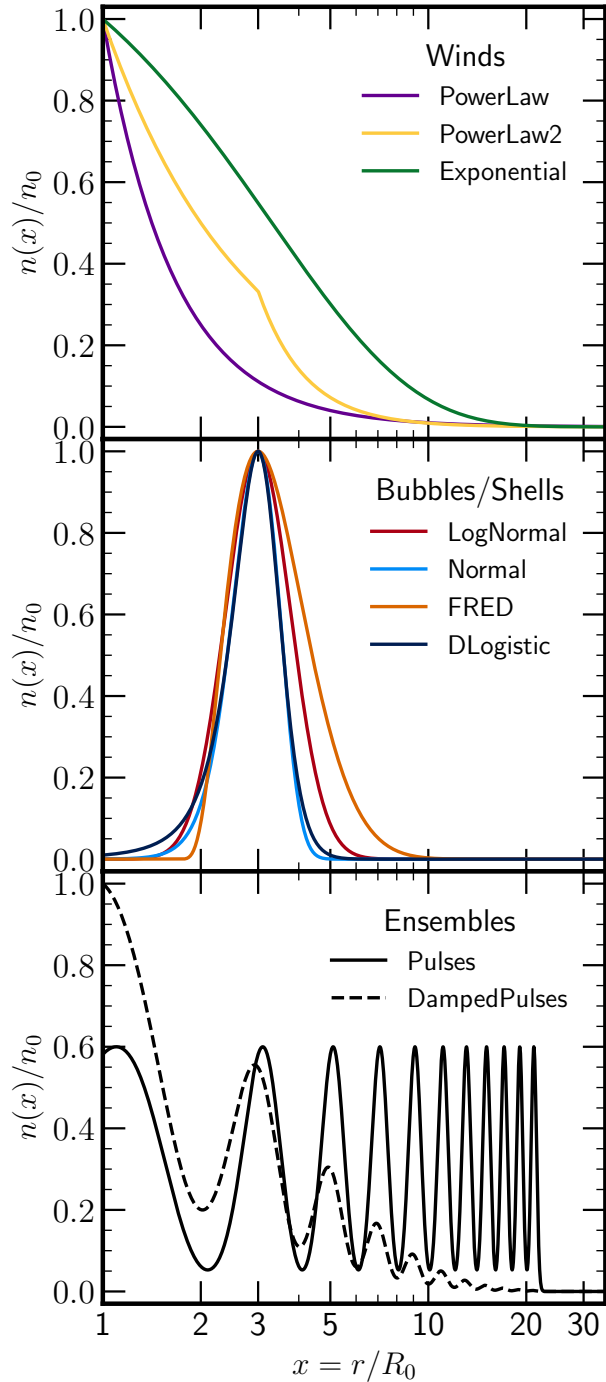


Figure 3. Radial density profiles included in OutLines and given by Equations 19–28. *Top:* Wind-like density profiles, including power law (‘PowerLaw’, purple, Eqn 19), double power law (‘DoublePowerLaw’, yellow, Eqn 21), and exponential (‘Exponential’, green, Eqn 20) distributions. *Center:* Pulse-like density profiles, including the normal (‘Normal’, blue, Eqn 22), log normal (‘LogNormal’, red, Eqn 23), fast-rise exponential decay (‘FRED’, orange, Eqn 24), and derivative of the logistic (‘DLogic’, indigo, Eqn 25) distributions, represent physical scenarios such as blast waves, expanding shells, and single burst events. *Bottom:* Ensembles of pulse-like profiles without (black solid, Eqn 27) and with (black dashed, Eqn 28) damping. These ensembles represent the resolved elements of a radially clumpy wind or a series of outflowing episodes.

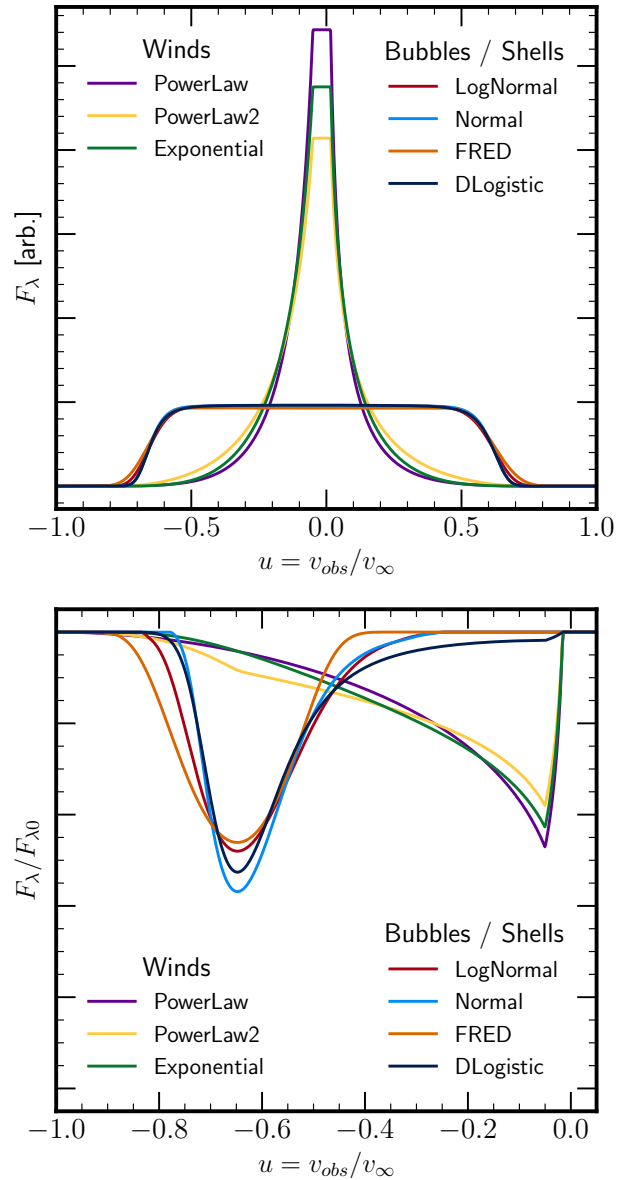


Figure 4. Nebular emission (*top*) and absorption (*bottom*) line profiles predicted by OutLines for fixed flux, column density, and velocity field for different density distributions assuming a spherical geometry. Colors matched to the corresponding profiles in Figure 3.

The exponential and power law profiles can be considered a combination of many instantaneous wind ‘pulses’ or multiple expanding shells, together resulting in a nearly continuous flow which in reality consists of multiple bursts. A prime example of this multi-episode flow phenomenon in nature is the consecutive shells observed in Wolf-Rayet nebulae like WR140, where traces of the individual pulses dissipate on the timescales much shorter than that of the outflow, producing a decline in flux comparable to an exponential or power law density profile (Lieb et al. 2025). Similar evidence is found from spectroscopy of the base or launch site of outflows, where successive episodes begin to resemble a continuous density distribution, as in the case of the Ly α and C IV lines in NGC 3783 (e.g., Mehdipour et al. 2017, 2025), and may even indicate an outflow or wind in formation. Alternatively, a system with multiple expanding

shells might appear as a series of pulses even when not spatially coincident (i.e., not nested), as in the case of starburst galaxies (e.g., [Rivera-Thorsen et al. 2015](#)). To that end, we also include density profiles for a series of pulse-like episodes (shells, bubbles, etc) such that, for N_p total pulses,

$$n[x] = \left(2\pi\sigma_x^2\right)^{-1/2} \sum_{i=0}^{N_p} \exp\left[-\frac{(x-x_1-ix_k)^2}{2\sigma_x^2}\right], \quad \text{Pulses} \quad (27)$$

where σ_x is the width of each pulse, x_1 is the radius of the smallest pulse (akin to a phase shift) and x_k is the interval spacing between pulses. We assume N_p such that pulses span the observationally relevant velocity field from $x = 1$ to $x[0.95]$ for any given x_1 and x_k . To allow pulses to relax or dissipate over time, we also include a damped pulse series

$$n[x] = \frac{\exp[-\gamma x]}{\sqrt{2\pi\sigma_x^2}} \sum_{i=0}^{N_p} \exp\left[-\frac{(x-x_1-ix_k)^2}{2\sigma_x^2}\right], \quad \text{DampedPulses} \quad (28)$$

which is likely a more physical representation of outflows in formation. We show the effects of a series of pulse-like events or damped pulses on the emergent line profiles in [Figure 5](#) for shells resolved and unresolved in velocity. [Figure 5](#) illustrates how infinitely thin shells with infinitely small separations ($\sigma_x, x_k \rightarrow 0$) or relatively thick shells ($\sigma_x \gtrsim x_k$) produce a wind-like profile.

One might invoke the central limit theorem to argue that a system of many shells or bubbles will result in a Gaussian line profile; however, we find that neither the damped nor undamped pulses behave in this manner. Indeed, [Tenorio-Tagle et al. \(1996\)](#) find that *only* a Gaussian velocity field will produce an intrinsically Gaussian line profile for a sum of many shells, a scenario which does not appear to be consistent with the bulk motion of gas predicted by theory. They further demonstrate that profiles might only appear Gaussian due to smearing by a line spread function. These results are consistent with comparisons of integrated and spatially resolved observations of the ensemble of expanding shells in 30 Doradus where the bulk velocity field produces a line profile with a Gaussian-like core but distinctly non-Gaussian wings ([Chu & Kennicutt 1994](#)).

In all cases, simple algebra gives the density in the wind as a function of velocity. As the density term n_0 simply scales the total line profiles in our formalism below, the n_0 is absorbed into column density N_0 and flux F_0 terms, respectively.

2.4 Geometry

For any given radial velocity w , line emission or absorption is distributed evenly across a given projection angle ϱ (the polar coordinate), which we illustrate here under full special relativistic treatment. The special relativistic velocity projection of w in an arbitrary polar direction ϱ' in the observer's frame incorporates both longitudinal and transverse effects such that, following [Einstein \(1905, their §7\)](#),

$$\lambda = \lambda_0 \gamma (1 + \omega \cos \varrho') \quad (29)$$

where $\omega = w v_\infty/c$ and $\gamma^{-1} = \sqrt{1 - \omega^2}$ is the Lorentz factor. Additionally from §7 of [Einstein \(1905\)](#), the angle ϱ in the source frame requires a relativistic aberration correction to the observer's frame ϱ' , with a differential which reduces to

$$\sin \varrho' d\varrho' = \left(\frac{\lambda_0}{\lambda}\right)^2 \sin \varrho d\varrho. \quad (30)$$

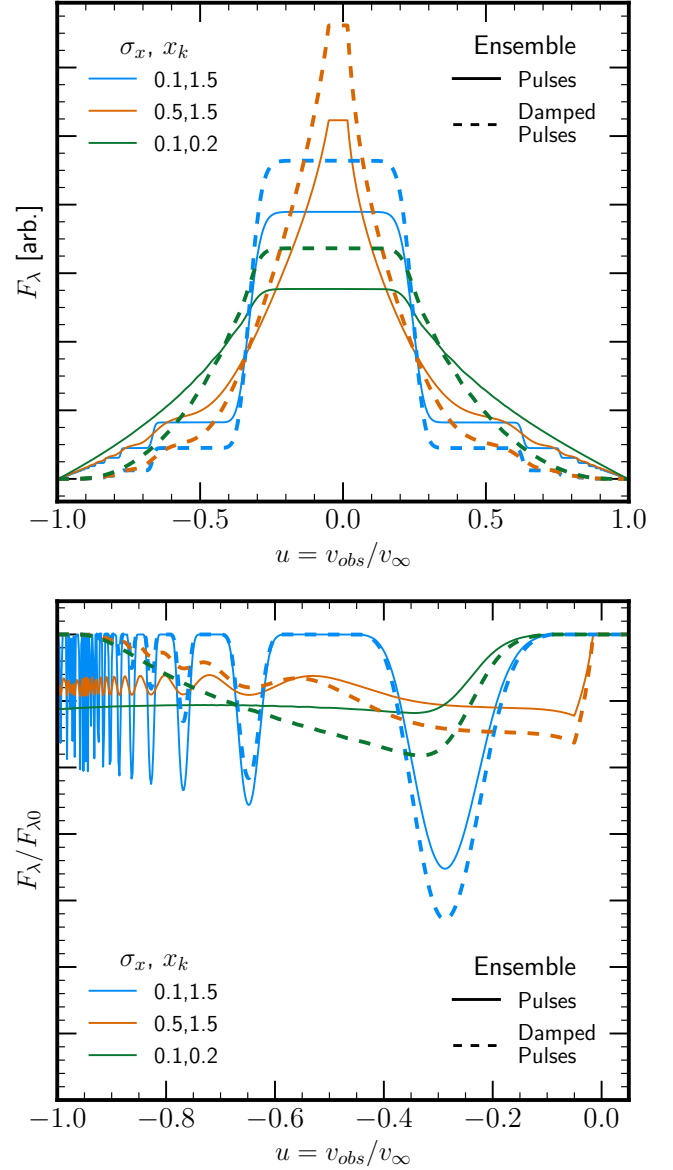


Figure 5. Nebular emission (*top*) and absorption (*bottom*) line profiles predicted by OutLines for an ensemble of expanding bubbles, shells, or other pulse-like episodes in cases of thick (orange, $\sigma_x = 0.5$) or thin (blue, $\sigma_x = 0.1$) widely-spaced shells and thin closely-spaced shells (green, $x_k = 0.2$) with (dashed) and without (solid) damping to mimic the effects of dissipation. In all cases, density, column density, velocity field, and terminal velocity are fixed, and a spherical geometry is assumed.

Combining these identities and respective differentials with Equation 1 provides a convenient substitution for the $\sin \varrho d\varrho$ term in $d\Omega$ such that

$$d\Omega' = 2\pi \frac{\sqrt{1 - \omega^2}}{\omega(1 - \omega)^2} \sqrt{\frac{1 - \omega}{1 + \omega}} d\omega \quad (31)$$

where 2π is the integrated azimuthal angle assuming any given de-projected velocity ω is fully inscribed by the outflow (a spherical geometry) – we return to adjust this assumption later. In the classical limit of $\omega \ll 1$, the differential solid angle reduces to $d\Omega = 2\pi/w dw$, the classical solution given by [Beals \(1931\)](#). This $d\omega$ substitution for $d\Omega$ is key to solving Equations 5 and 10 as it allows the line profile

to be expressed solely in terms of differential velocity (e.g., [Castor & Lamers 1979](#)). The implication, here, is that a shell with smaller velocity (and thus smaller radius) contributes more to the differential surface area.

To illustrate the effects of assumed velocity field and related $\cos \varrho$ projection onto the line of sight, we illustrate contours of constant observed velocity (isocontours) in Figure 6 (see also [Castor 1970](#), their Figure 1, [Lucy 1971](#), their Figure 2). Sometimes referred to as velocity surfaces (as in [Castor 1970](#)), these isocontours represent the velocities which are cosine projected to a single observed velocity, assuming a particular velocity field and varying the power law index.

2.4.1 Velocity Limits

The weighted contributions of each deprojected velocity to the absorption or emission allows us to reduce the geometry to the velocity limits w_ℓ and w_u of the integrals in Equations 5 and 10. Boundary conditions for velocity in the case of a uniform spherical outflow (illustrated in Figure 7) are given by some minimum and maximum projected velocities w_ℓ , w_u , respectively. The lower limit w_ℓ is simply the observed velocity $|u|$ for a uniform sphere if no obstruction occurs. From Figure 7, the line-emitting gas posterior to the source (redshifted in the case of an outflow) cannot be seen by the observer, meaning that w_ℓ must account for obstruction by the launching source at $x = 1$. Solutions for the source obstruction velocity limit are given in [Flury et al. \(2023\)](#), which we summarize here. From the Pythagorean theorem, the minimum velocity w_ℓ must satisfy

$$w_0 = |u| \frac{x[w_0]}{\sqrt{x^2[w_0] - 1}} \quad (32)$$

giving a lower velocity limit of

$$w_\ell = \begin{cases} |u| & \text{no source effect} \\ w_0 & \text{source effect} \end{cases} \quad (33)$$

where the ‘source effect’ applies only for the line-emitting gas posterior to the launch site relative to the observer (left half of the isocontours in Figure 6, of the sphere in Figure 7, and of the cartoon in Figure 10).

In principle, the upper velocity limit is simply the terminal velocity, i.e., $w_u = 1$. However, the spectroscopic aperture might not capture the full extent of the outflow. This aperture clipping effect is most likely to affect emission line profiles as the core arises from extended material. OutLines incorporates aperture clipping into the geometry as some maximum velocity v_a captured by the spectroscopic aperture on the transverse axis (plane of the sky) assuming that (i) the aperture is circular, as is the case for fiber spectrographs, and (ii) the outflow source is perfectly centered within the aperture. This effect can be imposed via the integral limits relative to the terminal velocity as $w_a = v_a/v_\infty$. The corresponding limiting velocity can be written as

$$w_1 = |u| \frac{x[w_1]}{\sqrt{x^2[w_1] - x^2[w_a]}} \quad (34)$$

following the same approach as with w_0 in Equation 32. We show the change in w_1 for different w_a in Figure 9 and illustrate the effect of aperture clipping for different w_a in Figure 8.

The limit of w_a most dramatically affects the projected velocities close to the transverse axis. As a result, aperture clipping will predominantly truncate the core of the profile close to the central wavelength (see also [Scarlata & Panagia 2015](#)); i.e., the broadest extent of the wings remains *relatively* unaffected. Moreover, absorption lines arise from gas anterior to the launch site that is backlit

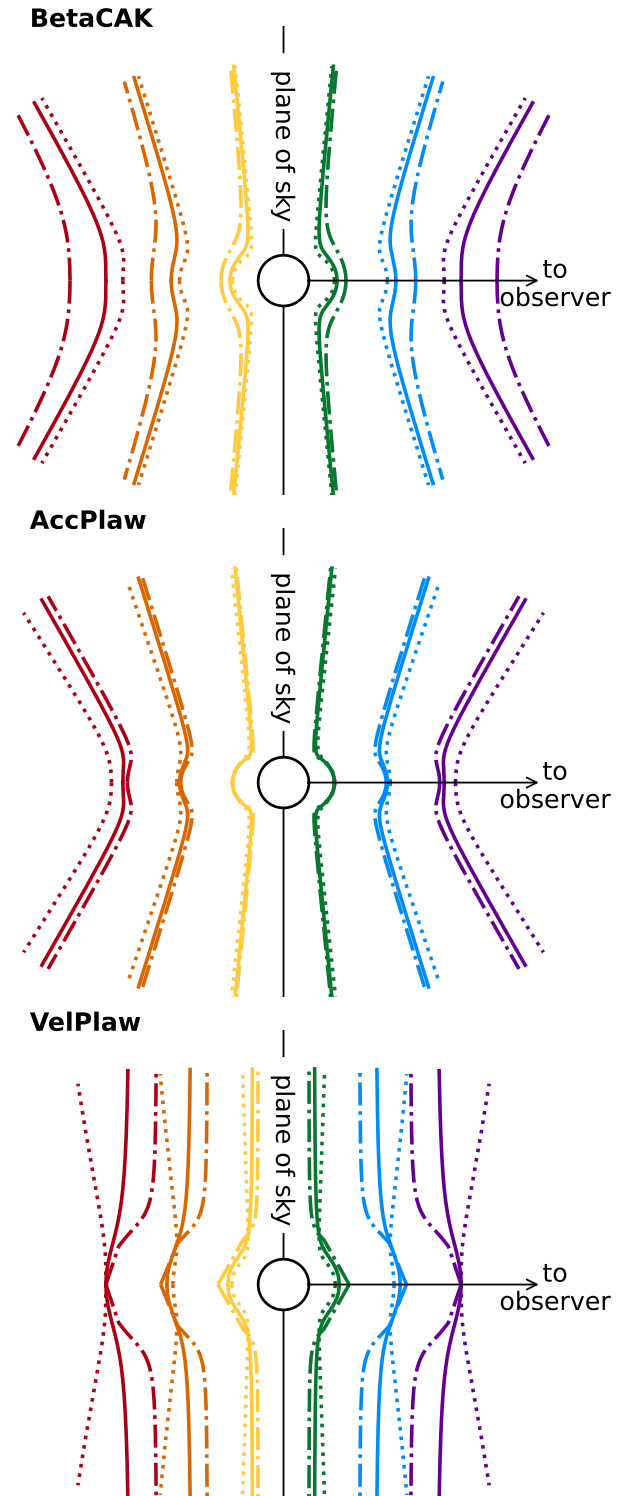


Figure 6. Velocity isocontours for the different velocity fields available in OutLines: the β law approximation to CAK theory (*top*), an acceleration power law (*middle*), and a velocity power law (*bottom*). Colors indicate fixed observed velocities of $v_{obs}/v_\infty = u = 0.1$ (yellow/green), 0.3 (orange/blue), and 0.5 (red/purple). Line styles indicate low (dotted), intermediate (solid), and high (dash-dotted) values of β for each velocity field. Arrow indicates the direction towards the observer, with cool colors representing blue Doppler shifts and warm colors representing red Doppler shift.

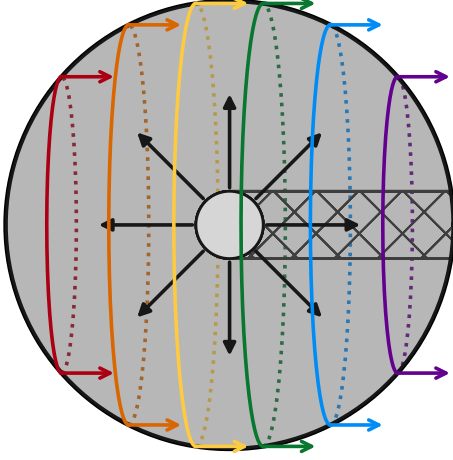


Figure 7. Spherically symmetric outflow presented in the text with a constant-velocity surface with a radius of u . Black arrows indicate the motion of the outflow. Central circle indicates the launching source of the outflow. Filled grey region indicates line-emitting material while the hatched region indicated line-absorbing material. Colored arrows indicate the direction of light propagation towards the observer. Colored circles indicate different deprojected velocities w which can contribute to a single observed velocity surface u with values of $u/w = 0.15, 0.5, 0.85$ corresponding to yellow/green, orange/blue, and red/purple, respectively.

by the source, resulting in a “pencil beam” effect where the maximum velocity contributing to the profile is w_0 (hatches in Figure 7). Combining w_1 and w_0 gives a final upper velocity limit of

$$w_u = \begin{cases} w_0 & \text{absorption} \\ w_1 & w_1 < 1 \\ 1 & \text{otherwise} \end{cases} . \quad (35)$$

We visualize the integral limits w_ℓ and w_u in Figure 9.

2.4.2 Directed Outflows

Many outflows are not spherically uniform but rather are observed as bi-directional cones on a wide variety of scales (e.g., Fukui et al. 1986; Clegg et al. 1987; Heckman et al. 1990; Colina et al. 1991; Hirano et al. 1992; Marlowe et al. 1995; Cameron et al. 2021). We consider a bi-directional conical geometry with a half opening angle θ_o and an inclination angle i with respect to the observer, which we depict in Figure 10 (see also, e.g., Figure 5 in Hjelm & Lindblad 1996). OutLines includes a tool `PlotGeometry` for producing such figures as a visual aid.

The major difference with conical geometry is that the polar coordinate of the differential solid angle $d\Omega$ now depends on i and θ ; we cannot simply assume each deprojected velocity contributes equally to the integral due partial coverage. Therefore, we must account for azimuthal angle of the deprojected velocity which falls within the region of the cone projected onto the plane of the sky. The azimuthal angle inscribed by the projected cone simply scales the total solid angle by a factor $\ell_w(u, w, i, \theta) \in [0, 1]$ to give the relative contribution of a de-projected velocity w to the observed velocity u . OutLines computes the conical projection from i, θ_o and then calculates ℓ_w by determining the angular length(s) of each deprojected velocity inscribed by the projected cone. For details on this method, we refer

the reader to Appendix A (see, e.g., Zheng et al. 1990; Carr et al. 2018; Luminari et al. 2018, for earlier approaches to solving this problem). We illustrate the effects of changing the opening angle θ_o and inclination angle i in Figure 11.

2.4.3 Directed Outflows with Cavities

An additional geometry observed in young stellar objects (e.g., Padgett et al. 1999; Louvet et al. 2018; de Valon et al. 2020), stellar winds (e.g. Sirianni et al. 1998), starbursts (e.g., Axon & Taylor 1978; Marlowe et al. 1995; Heckman et al. 1995; Rich et al. 2010; Yoshida et al. 2011), and AGN (e.g., Phillips et al. 1983; Hjelm & Lindblad 1996; Crenshaw & Kraemer 2000; Crenshaw et al. 2000; Müller-Sánchez et al. 2011; Venturi et al. 2018) is that of hollow cones of outflowing material. We include this geometry, assuming some cavity angle θ_c and opening angle θ_o (see also models by Das et al. 2006; Müller-Sánchez et al. 2011; Bae & Woo 2016; Luminari et al. 2024). OutLines implements this geometry by subtracting the fractional angular length ℓ_{cavity} of each deprojected velocity inscribed by the cavity from the angular length inscribed by the total cone (see Appendix A). The difference will always be positive and greater than zero since $\theta_o > \theta_c$ by definition. We illustrate the impact of a hollowing of the outflow cone on the emergent line profile in Figure 12. Somewhat intuitively, an edge-on hollow-cone outflow loses flux from the least Doppler-shifted gas (truncating the core) while a face-on hollow-cone outflow loses flux from the most Doppler-shifted gas (truncating the wings).

2.4.4 An Obstructing Disk

The outflow may be launched from a region embedded in a disk of optically thick material, a phenomenon observed in a variety of astrophysical scenarios: expelled debris in planetary nebulae (e.g., Icke 1981), protoplanetary material around young stellar objects (e.g., Padgett et al. 1999; Ilee et al. 2016), the dusty material concentrated around an AGN (e.g., Veilleux et al. 2001), or even the plane of a galaxy (e.g., Hjelm & Lindblad 1996; Cronin et al. 2025). In such cases, the disk will obstruct some of the observer’s view of the outflow. OutLines optionally includes obstruction by a circular disk which is orthogonal to the central axis of the cones and which has some radius $x_d = r_{\text{disk}}/R_0$. As with the cones, the disk must be projected onto the plane of the sky and subsequently compared to the deprojected velocity inscribed by the projected cone to determine the fractional arc length(s) ℓ_w inscribed by the cone but not the projected disk. We elaborate on this formalism in Appendix A. OutLines implements a disk either in tandem with the cone geometries or alone as a hemisphere geometry.

We illustrate the effects of including an obstructing disk for the hemisphere and bidirectional cone cases in Figure 13 and for the bidirectional cones in Figure 14. By definition, the disk will only obstruct the posterior cone, so if $i + \theta_o < 90^\circ$, the disk will only obstruct the receding outflow, solely obstructing the redshifted component (left of Figure 14). However, when $i + \theta_o > 90^\circ$, the disk obstructs the lune projected by the posterior cone toward the observer, resulting in loss of the blueshifted component of the line profile as well (right of Figure 14).

2.5 Outflow Properties

Following Flury et al. (2023, see their Appendix B), the characteristic outflow radius x_{out} corresponds to the maximum momentum density

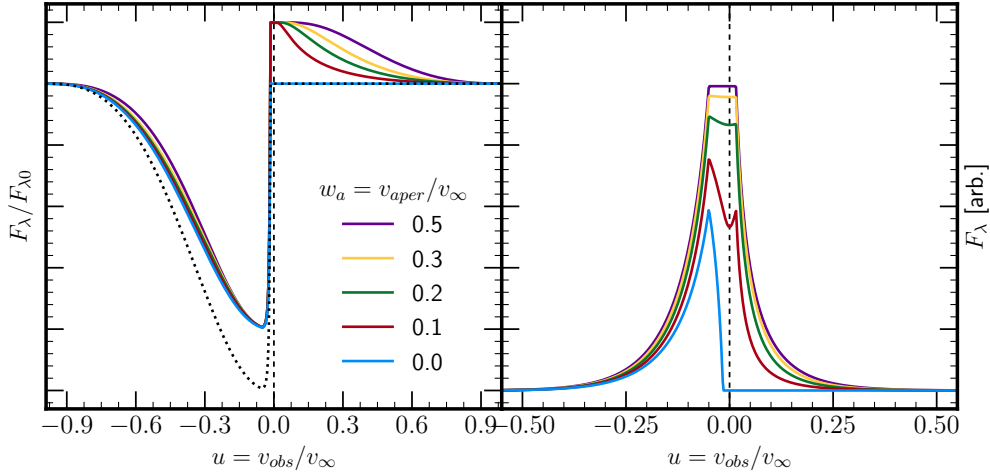


Figure 8. Effect of aperture clipping on the observed line profile for a P Cygni line consisting of absorption and resonant emission with filling factor $\epsilon = 0.2$ and escape fraction $p_{res} = 1$ (left panel) and for nebular emission (right panel). For visualization, lines are normalized to the case of no aperture clipping ($w_a = 1$). Dotted black line in the left panel indicates pure absorption, demonstrating that infilling can still occur in the fully aperture-clipped limit but that only an absorption profile is observed (cf. [Scarlata & Panagia 2015](#)). Note that the effect of radiative trapping on the resonant line core decreases as w_a decreases.

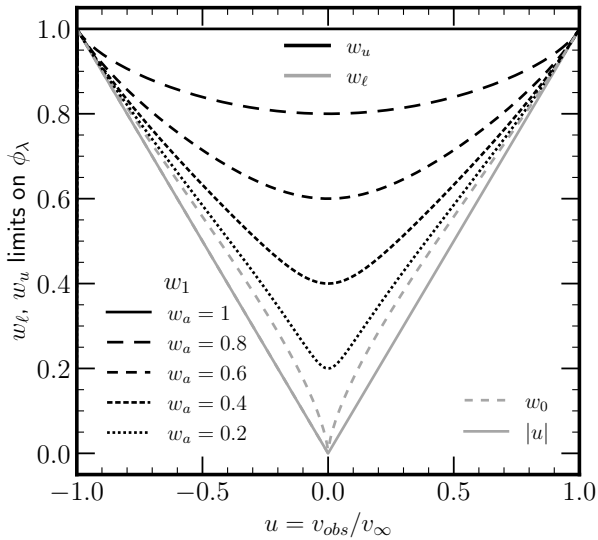


Figure 9. Integral velocity limits for the emission line profile ϕ_λ . Lower limit w_ℓ is shown in grey with (dashed, w_0 , Equation 32) and without (solid, $|u|$) the outflow source. Upper limit w_u is shown in black with (dashed, w_1 , Equation 34) and without (solid, unity) aperture clipping.

$\dot{\rho}_p = \mu m_{\text{H}} n_0 v_\infty n[x] w[x]$, i.e., where the wind effects are strongest. In the case of pulse-like density distributions, the center of the gas distribution x_1 will be close to, but not always the same as, x_{out} . The radius x_{out} of maximum momentum density scales all other outflow properties, first and foremost the characteristic outflow velocity v_{out} by determining the velocity at x_{out} using the velocity field w such that

$$v_{\text{out}} = v_\infty w[x_{\text{out}}]. \quad (36)$$

The effective column density N_{out} at the characteristic radius can be determined by integrating over the density profile from the base of the outflow ($x = 1$) to the peak momentum density $x = x_{\text{out}}$

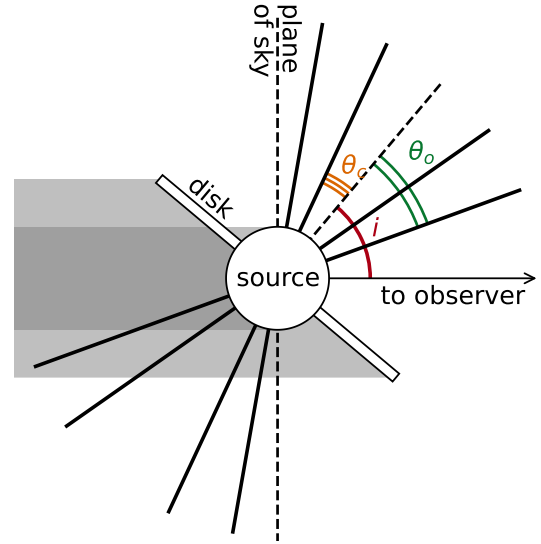


Figure 10. Outflow geometry accounting for obstruction by the outflow source (white circle with dark grey shaded region) and by an optional disk (rectangle with light grey shaded region). Red arc indicates the inclination angle i of the cone axis with respect to the observer. Green double arc indicates the opening angle θ_o of the cone between the axis and the edge. Orange triple arc indicates the optional cavity angle θ_c between the cone axis and the inner edge of the outflow.

(e.g., [Flury et al. 2023](#), their Equation 13 for the case of a CAK velocity field and power law density profile). Note that N_{out} is not to be confused with N from the absorption line profile, which is the total column density along the line of sight. N_{out} necessarily depends on the space density n_0 and the radius at the base of the outflow R_0 , which are unconstrained parameters in OutLines. As

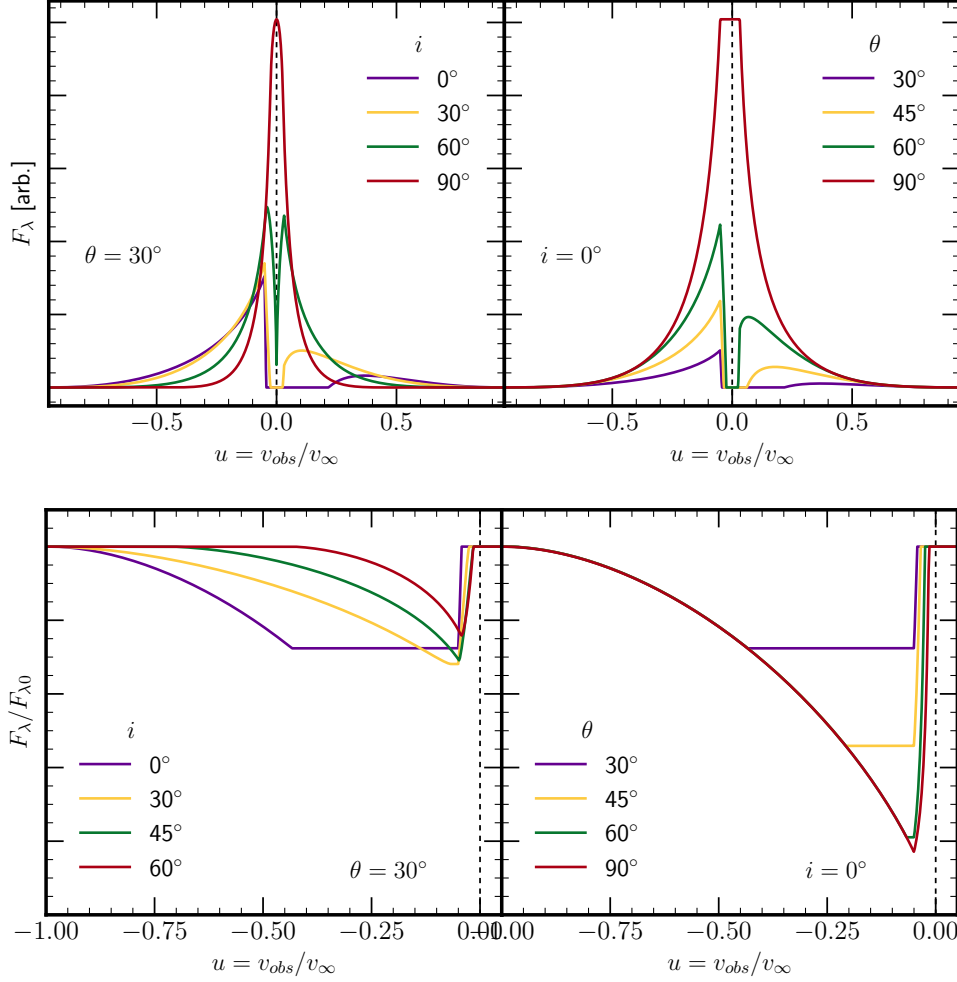


Figure 11. Effects of bi-directional conical geometry on the emergent line profiles of emission (top) and absorption (bottom) profiles for fixed density (power law with $\alpha = 2$) and velocity ($\beta = 1$) fields. To illustrate the effects of geometry, we either vary the inclination with respect to the observer (left) from face-on ($i = 0^\circ$) to edge-on ($i = 90^\circ$) with fixed opening angle of $\theta = 30^\circ$ or vary opening angle of the cones (right) from narrow ($\theta_o = 30^\circ$) to a full sphere ($\theta = 90^\circ$) with face-on inclination. The case of $i = 0$ and $\theta = 90^\circ$ (red line, right) is consistent with a filled sphere. For visualization, line profiles are all normalized to the spherical case ($i = 0^\circ$, $\theta = 90^\circ$). The effects of inclination on the emergent line profile shown in the upper left are similar to the 3D Monte Carlo simulation predictions for X-ray fluorescent lines from the `skirt` code (Vander Meulen et al. 2024; Bianchi et al. 2026), with face-on inclination yielding broader and flatter profiles and edge-on inclination yielding narrower and peakier profiles.

such, OutLines computes the relative column density \mathcal{R} where

$$\frac{N_{\text{out}}}{n_0 R_0} = \mathcal{R} = \int_1^{x_{\text{out}}} n[x] dx. \quad (37)$$

This quantity \mathcal{R} becomes important for computing the strength of the outflow expressed via \dot{M} , \dot{p} , and \dot{E} .

The mass outflow rate \dot{M} is given by the momentum flux $\mu_{\text{H}} n_0 v_{\text{out}}$ with a geometric projection $4\pi R_0^2 (\cos \theta_c - \cos \theta_o)$ such that

$$\dot{M} = 4\pi (\cos \theta_c - \cos \theta_o) n_0 R_0^2 \mathcal{R} \mu_{\text{H}} v_{\text{out}}, \quad (38)$$

a more general case of Equation 12 from Flury et al. (2023). Such formalism is frequent in the literature with differences in implementation of the geometric projection (e.g. Rupke et al. 2005a,b; Crenshaw & Kraemer 2012; Maiolino et al. 2012; Fiore et al. 2017; Luminari et al. 2018, 2024; Flury et al. 2023). The outflow momentum rate \dot{p} expresses the rate at which momentum is injected into the outflow.

Typically, \dot{p} is defined as the product of outflow velocity and mass outflow rate (e.g., Rupke et al. 2005b, their Equation 9) such that

$$\dot{p} = v_{\text{out}} \dot{M} = 4\pi (\cos \theta_c - \cos \theta_o) n_0 R_0^2 \mathcal{R} \mu_{\text{H}} v_{\text{out}}^2. \quad (39)$$

The outflow mechanical luminosity \dot{E} expresses the injection of kinetic energy into the outflow. Typically, \dot{E} is defined as the product of outflow velocity and mass outflow rate (e.g., Rupke et al. 2005b, their Equation 11) such that

$$\begin{aligned} \dot{E}_{\text{out}} &= \frac{1}{2} \dot{M} (v_{\text{out}}^2 + 3\sigma_v^2) \\ &= 2\pi (\cos \theta_c - \cos \theta_o) n_0 R_0^2 \mathcal{R} \mu_{\text{H}} (v_{\text{out}}^3 + 3v_{\text{out}}\sigma_v^2). \end{aligned} \quad (40)$$

These values can be readily computed using constraints on x_{out} and v_{∞} and possible geometric terms θ_o and θ_c , all obtained from the line profile. The only two unknowns are n_0 and R_0 , which cannot be directly informed by the line profile and require additional measurements (spatial for R_0 , spectral for n_0) or assumptions based on prior knowledge. For instance, $n_0 = 10 \text{ cm}^{-3}$ and $R_0 = 0.5 \text{ kpc}$ may

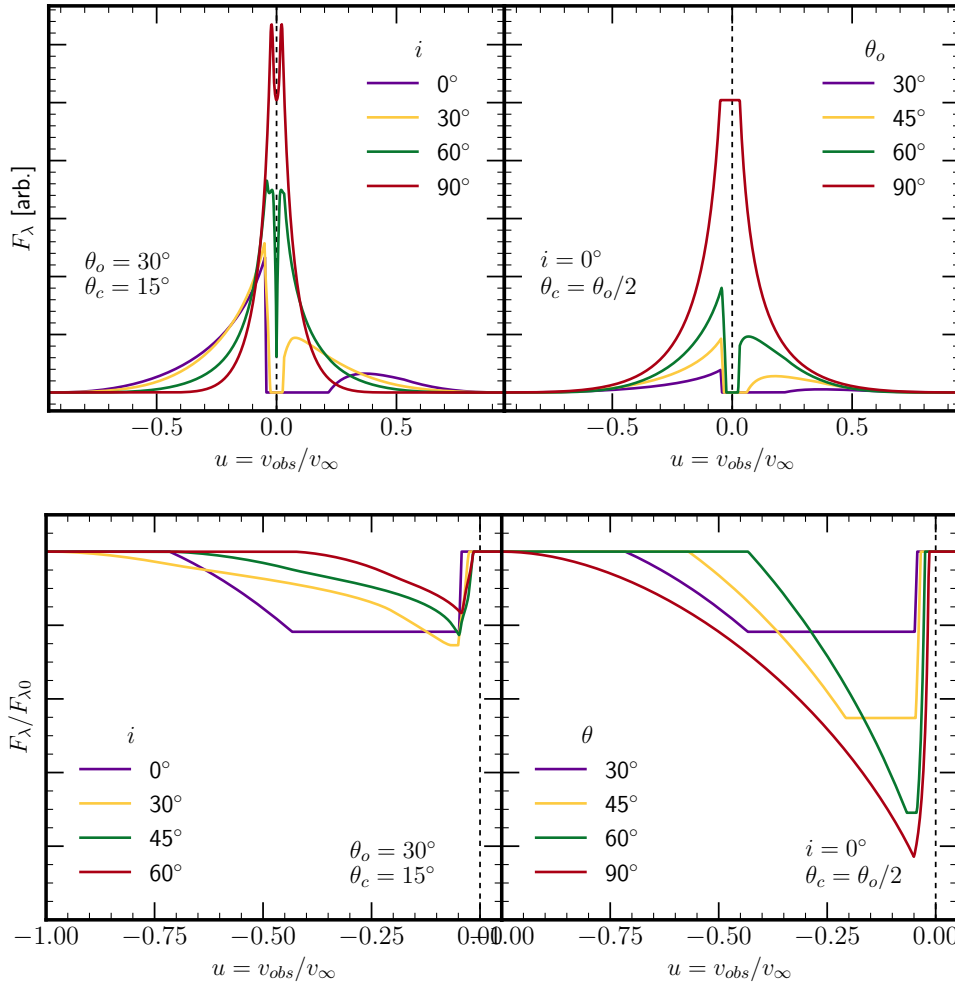


Figure 12. Same as Figure 11 but for hollow bi-directional cones with cavity angle $\theta_c = \theta_o/2$.

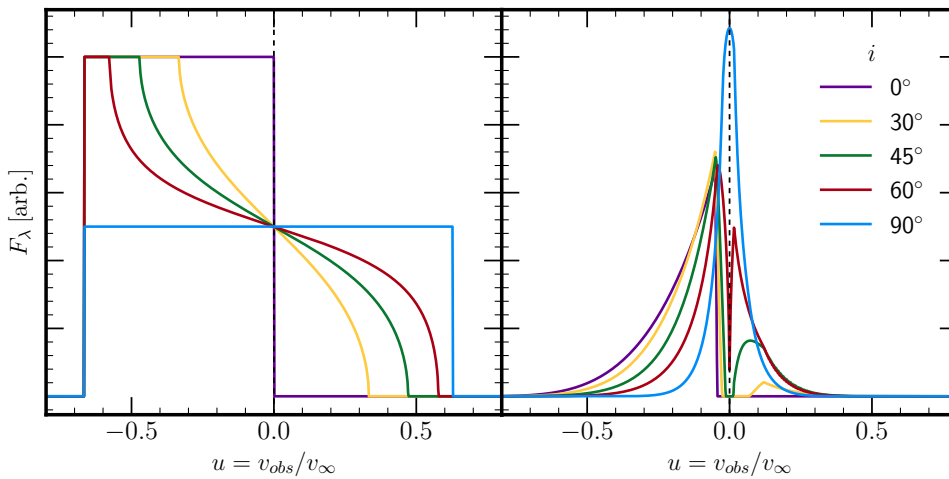


Figure 13. Same as Figure 11 but for the effects of an obstructing disk as a function of inclination with respect to the observer in (left) a thin single-shell hemisphere geometry where all material posterior to the disk is obstructed (cf. [Xrism Collaboration et al. 2025](#), their Fig 12) and (right) a biconical wind with $\theta_0 = 30^\circ$ and $x_{\text{disk}} = 5$. Colors indicate changes to the inclination angle i , illustrating the redistribution of flux from entirely blue-shifted ($i = 0^\circ$) to evenly blue- and red-shifted ($i = 90^\circ$).

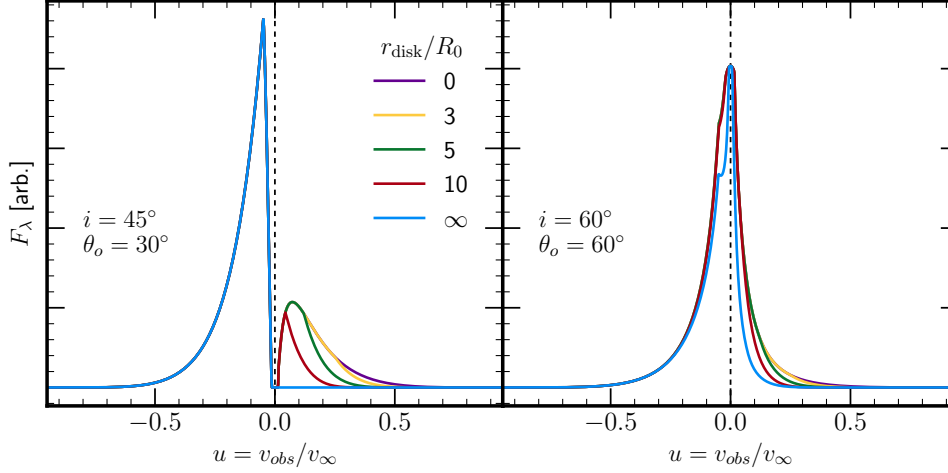


Figure 14. Same as Figure 11 but for bidirectional cones with fixed inclination and opening angle and an obscuring disk with varying radii, where a radius of 0 indicates a disk-free line profile. All profiles are normalized to the disk-free case for illustrative purposes. On the left, $i + \theta_o < 90^\circ$, resulting in loss of the redshifted component. On the right, $i + \theta_o > 90^\circ$, resulting in losses of both red- and blueshifted components when the disk radius is sufficiently high. For visualization, line profiles are normalized to the disk-free case in each panel.

be reasonable for galactic outflows (e.g., Chevalier & Clegg 1985; Flury et al. 2023).

As implemented here, we compute \dot{M} , \dot{p} , and \dot{E} normalized to $n_0 R_0^2$ with n_0 in cm^{-3} and R_0 in kpc, meaning the characteristics of the outwardly moving gas are written as

$$\frac{\dot{M}}{M_\odot \text{ yr}^{-1}} \left[\frac{n_0 R_0^2}{\text{cm}^{-3} \text{ kpc}^2} \right]^{-1} = 0.191 \mathcal{R} [\cos \theta_c - \cos \theta_o] \left[\frac{v_{\text{out}}}{\text{km s}^{-1}} \right] \quad (41)$$

$$\frac{\dot{p}}{\text{dyne}} \left[\frac{n_0 R_0^2}{\text{cm}^{-3} \text{ kpc}^2} \right]^{-1} = 10^{-3.2} \left[\frac{v_{\text{out}}}{\text{km s}^{-1}} \right] \left[\frac{\dot{M}}{M_\odot \text{ yr}^{-1}} \right] \quad (42)$$

$$\frac{\dot{E}}{\text{erg s}^{-1}} \left[\frac{n_0 R_0^2}{\text{cm}^{-3} \text{ kpc}^2} \right]^{-1} = 10^{-6.5} \left[\frac{v_{\text{out}}}{\text{km s}^{-1}} \right]^2 \left[\frac{\dot{M}}{M_\odot \text{ yr}^{-1}} \right] \quad (43)$$

Typically, $n_0 R_0^2$ is of order unity for the case studies in §4, with values ranging from about 1 to $5 \text{ cm}^{-3} \text{ kpc}^2$, although for Mrk 462, Flury et al. (2023) find $n_0 R_0^2 = 12 \text{ cm}^{-3} \text{ kpc}^2$.

3 THE OUTLINES CODE

OutLines, a portmanteau of outflows and spectral lines, implements all of the above model components in a single code for emission and absorption lines. The code is designed to be simultaneously efficient and user-friendly, with a straightforward user interface and ready scientific application. Below, we assess OutLines in the contexts of standard techniques, including empirical percentiles and multi-Gaussian fitting. Details of the architecture and use of the OutLines code can be found in Appendix B with additional examples available in Jupyter notebooks online at <https://github.com/sflury/OutLines>.

3.1 Empirical Percentiles

The empirical approach of velocity percentiles (e.g., Heckman et al. 1981; Whittle 1985; Veilleux 1991; Rupke & Veilleux 2013; Liu

et al. 2013; Veilleux et al. 2020) measures the velocity at which the cumulative flux or equivalent distribution reaches some percentile. OutLines provides quantiles of individual model line profiles through the `velocity_quantiles` method bound to the line profile object class and a convenience function `get_W80`, a common interval in the literature (e.g., Harrison et al. 2014; Fiore et al. 2017), which returns the W80 value from the 10-90 percentiles. While OutLines includes a `get_FWHM` function similar to the full-width at half-maximum (FWHM), this function is the velocity width of the profile containing the inner 50% of the flux (W_{50}) and can be thought of as the full-width at half-flux (FWHF) centered on the first moment (median) of the flux distribution. We note that the FWHM can be somewhat misleading, particularly in cases of a high velocity outflow where the flux density is low relative to the maximum and would not be represented by the FWHM velocity (see Fig 15) or could yield multiple values in cases where the outflow component is multi-peaked. Illustrations of the 1σ and 2σ quantiles for an absorption and emission line with the OutLines defaults for filled cone geometry and a static component are shown in Figure 15.

3.2 Modeling Line Profiles

Given that OutLines will sometimes require a large number of parameters (anywhere from four to nine for a given line depending on the geometry and density profile), we strongly recommend the use of Markov-chain Monte Carlo (MCMC) or other Gaussian-process samplers of the posterior on the parameters rather than the various least squares minimizers. Not only can this improve fit results but also allow users to incorporate informative priors, plus marginalization of particular nuisance parameter, which the trust-reflective algorithm, Levenberg-Marquardt, and other nonlinear least squares routines cannot. E.g., in the hollow cone scenario, $\theta_o > \theta_c$ necessarily and should be enforced.

To facilitate modeling of observed line profiles, the `Profile` classes contain several attributes and functions. Users can access the model line profile function directly via the `Profile` attribute, which receives rest wavelengths and parameters from the user and returns the total line profile predicted by the OutLines code.

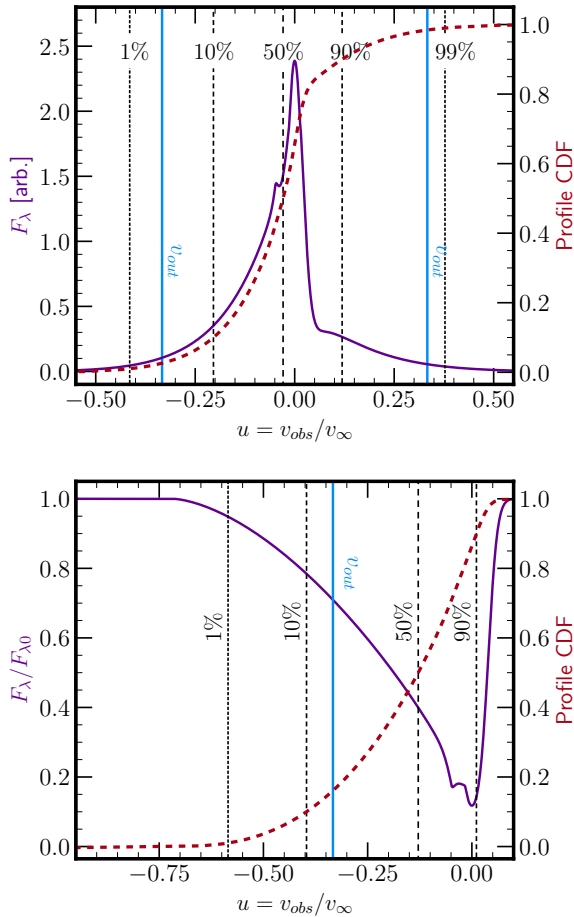


Figure 15. Velocity percentiles (black dashed lines) for an arbitrary emission (*top*) and absorption (*bottom*) line (purple) generated by `OutLines` for a directed, filled cone geometry (Geometry='FilledCones') for $i = 45^\circ$ with $v_0 = 0.1v_\infty$ (FromRest=False), default parameters, and otherwise default settings. The cumulative distribution function (fraction of integrated flux) is shown in red. For reference, we show the characteristic outflow velocity v_{out} (Equation 36) in blue.

When instantiated, the `Profile` classes also contain initial parameter guesses and boundaries accessible via the `get_params()` and `get_bounds()` methods. For convenience, these two classes also contain the `init_params` function which will sample walkers within the current parameter bounds given the current parameter values. These initial parameter guesses can be readily seeded into an MCMC sampler while the boundaries can be folded into a prior. For this purpose, the `log_probability()` bound method includes both the likelihood and a uniform bounded prior incorporating the boundary values contained in the object. Users are able to update any or all of these bound methods as needed. An example of modeling with `OutLines` is provided in Appendix D.

While we encourage simultaneous fitting of multiple features from the same or very similar species, we caution against modeling lines from different species which may not necessarily share, say, the same density profile parameters due to ionization structure within a multiphase outflow.

`OutLines` does not presently include line-spread function (LSF) corrections in-house: such corrections are left to the user at this time. To assess the impact of the LSF on the recovery of line profiles,

we generate 10^4 mock observations varying R from 1 000 to 10 000, v_∞ from 100 to 1 000 km s^{-1} , and β from 0 to 2.5 assuming the `OutLines` defaults. We convolve the predicted line profiles with a Gaussian LSF and add noise consistent with S/N between 3 and 10 in the continuum. We fit the mock observations using the `scipy.least_squares` trust reflective algorithm to attempt to recover the input parameters. Our simulation indicates that $R \sim 1500$ is sufficient to recover outflow properties to within $\lesssim 15\%$ with a simple Gaussian LSF correction and $R \sim 3000$ to within 10%, suggesting that facilities such as *JWST/NIRSpec* can be used with `OutLines` to recover key information about winds, bubbles, and outflows. Moreover, we find that $R \sim 6000$ can recover parameters within $\approx 5\%$ of the input values even without an LSF correction, suggesting LSF corrections in this regime are negligible.

We illustrate the importance of using `OutLines` over traditional methods by comparing a fit to a mock [O III] $\lambda 5007$ line profile at $R = 5\,000$ with Nyquist sampling and S/N = 10 at the peak flux with `OutLines` and with a double Gaussian, both of which we show in Figure 16. For this purpose, we generate a mock line profile using `OutLines` for an acceleration power law velocity field with $\beta = 1.5$ and $v_\infty = 500 \text{ km s}^{-1}$, power law density profile with $\alpha = 1$, and filled cone geometry with $i = 45^\circ$ and $\theta_o = 30^\circ$. We add a static component with $\sigma_v = 50 \text{ km s}^{-1}$. Both the static and outflow components have equivalent integrated fluxes normalized to unity in the mock profile.

Overall quality of the best-fit profile we obtain is comparable ($\chi^2 = 2.057$ and 2.942 for `OutLines` and a double Gaussian, respectively). The double Gaussian model does have fewer parameters (6) than the `OutLines` model (9). Given the similarity in χ^2 , the difference in Akaike information criterion (AIC) between the `OutLines` and double-Gaussian model is dominated by the number of parameters, leading to $\Delta\text{AIC} = 6.7$. At face value, the AIC might favor the multi-Gaussian approach; however, the multi-Gaussian approach has no strong physical argument and, as we elaborate below, leads to spurious conclusions about the physical nature of the observed phenomenon. The AIC results are therefore more indicative of the shortfalls of relying solely on statistical metrics rather than physical motivation. In other words, all free parameters are equal, but some are more equal than others.

With this caveat in mind, we compare the results between the standard method and our new approach with `OutLines` in modeling an outflow. `OutLines` is able to recover all input parameters within the imposed 10% uncertainty due to noise. The double Gaussian model over-predicts the outflow flux by a factor of two and under-predicts the static gas flux by a factor of three while characterizing the outflow as red-shifted relative to the systemic velocity of the static gas. The double Gaussian model results lead to vastly different physical interpretations of the observations than those from `OutLines`: one would conclude the presence of a more massive outflow that is systematically traveling away from the static gas at 15 km s^{-1} , perhaps merger-like activity. One might even be inclined to interpret the double-Gaussian result as evidence for an inflow rather than an outflow, which is not the case. The `OutLines` best-fit model indicates an outflow launched from the same systemic velocity as the static gas with a bidirectional cone geometry and with characteristic velocities of $v_{\text{out}} = 220 \text{ km s}^{-1}$. Following Equation 38, accounting for the geometry (a factor of $1/(1 - \cos \pi/6) \approx 7.5$), differences in line flux ($n_0 \propto \sqrt{F_0}$ gives a factor $\sqrt{2}$), and difference in v_{out} (factor of 0.5), the double Gaussian model yields a mass loss rate higher than that of `OutLines` by a factor of five. Thus, while the velocity inferred from the double Gaussian model is half that from `OutLines`, the double

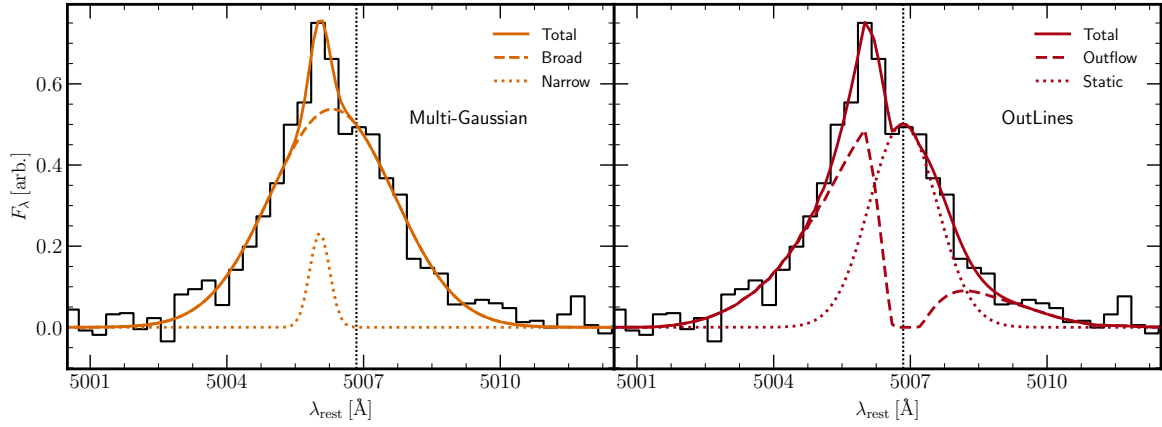


Figure 16. Fit to a mock [O III] $\lambda 5007$ outflow profile (see §3.2) with a double Gaussian (left) and with OutLines (right). While the fit quality is comparable in terms of χ^2 , the inferred fluxes and kinematics differ dramatically, leading to disparate scientific conclusions.

Gaussian model implies a substantially higher impact of the outflow on its environment than the OutLines model.

3.3 Absorption vs Emission

A key result of the development and applications of OutLines is that absorption and emission lines optimize constraints on different properties of outflows. Absorption lines are more sensitive to the line-of-sight, as evidenced in the line profiles (Figures 2 and 4) and the narrow range in velocities contributing to each wavelength bin due to the “down-the-barrel” effect (Figures 7 and 9), making them good probes of the density profile and velocity field but poor tracers of the geometry. Emission lines trace the global gas distribution since velocities from across the majority of the gas contribute to each velocity bin (Figure 9), making them good probes of the geometry (Figures 11, 12, 14) but, as a result, lose some constraining power on the density profile and velocity field. As such, combined modeling of both emission and absorption provides optimal constraints on the outflow properties.

4 A HIGH CAPACITY FOR SCIENCE

Below, we demonstrate application of OutLines to a variety of phenomena on different spatial and temporal scales, all involving astrophysical winds: stellar wind bubbles in the brightest cluster of the giant extragalactic H II region NGC 5471, radiative feedback and Lyman continuum escape from a super star cluster in Green Pea J1044+4012, blowout and the formation of a directed outflow in starburst Mrk 1486, and thermal/cosmic ray pressure from AGN-shocked bubbles in the Seyfert 2 nucleus of NGC 2992. Results from modeling these examples with OutLines are given in Table 1 and are discussed on a cases-by-case basis in the subsections below.

All modeling with OutLines is done here using `emcee` to sample the posterior on the parameters. The MCMC chain consists of a number of walkers equal to twice the number of free parameters plus one (the OutLines default), with each walker taking 10^3 steps with an additional 200 burn-in steps given the number of walkers (minimum of 10 walkers for at least 2000 individual burn-in steps), which we find to be sufficient to “forget” the initial guess parameters. The initial guess parameters, unless otherwise stated, are obtained

using the `scipy.optimize.least_squares` trust-reflective algorithm fit. The prior is assumed to be uniform bounded unless otherwise stated. We show posterior sampling for each case in Appendix E.

4.1 Evolution of H II Regions

H II regions are dynamic environments with radiation and winds from O and B stars shaping and enriching the proximal ISM. Winds launched from stars carry out recently formed metals dredged up to the surface and subsequently sweep up surrounding material. Radiation heats gas, often through photoionization, and imparts momentum to the ISM, which can result in additional launching or driving of winds, bubbles, and outflowing gas (e.g., Castor et al. 1975b; Weaver et al. 1977; Dyson 1977, 1979; Oey & Clarke 1997; Dopita et al. 2005). While stellar population models often contain predictions for these feedback effects (e.g., Leitherer et al. 1999, 2014; Eldridge et al. 2017; Byrne et al. 2022; Hawcroft et al. 2025), empirically constraining the kinematics and related mechanical feedback in H II regions remains an active area of research (e.g., models and simulations by Geen et al. 2020, 2023; Lancaster et al. 2025a,b) with implications for understanding chemical enrichment (e.g., Esteban & Peimbert 1995; López-Sánchez et al. 2007; Stock et al. 2011) and dispersal timescales (e.g., Dopita et al. 2005; Menon et al. 2024).

One such kinematically rich and complex system is the giant extragalactic H II region NGC 5471 located in M101. Many knots within this region exhibit broad and sometimes asymmetric nebular lines which cannot be described by a single Gaussian (e.g., Chu & Kennicutt 1986; Bresolin et al. 2020). To investigate the evolution of H II regions in this case-study, we apply OutLines to the [S II] $\lambda\lambda 6716, 6731$ doublet, which traces the density and kinematics of low ionization gas, in Knot A of NGC 5471, the brightest knot identified by Skillman (1985), as observed with the $R = 6000$ MEGARA IFU spectrograph on the Gran Telescopio Canarias (Arellano-Cordova in prep, PI Esteban). For our modeling, we use a $2.5''$ aperture extraction of the Knot A spectrum from the IFU cube. We obtain atomic data from NIST (Kramida et al. 2024) for wavelengths (Kaufman & Martin 1993) and spontaneous emission coefficients (transition probabilities) (Podobedova et al. 2009). We use collision strengths from Tayal & Zatsarinny (2010). First, we fit the adjacent featureless continuum with a third-order polynomial, an appropriate approximation in the case of extended H II regions which do not suffer appreciably

Table 1. Best-fit parameters and properties of test-case objects: Knot A of giant extragalactic H II region NGC 5471, super star cluster in the center of Green Pea J1044+3053, star-forming galaxy Mrk 1486, and Seyfert 2 NGC 2992. As discussed in §2.5, reported properties of \dot{M} , \dot{p} , and \dot{E} are normalized to $n_0 R_0^2$ with n_0 in units of cm^{-3} and R_0 in kpc (see Equations 41–43).

Object	NGC 5471 Knot A		J1044+0353 SSC		Mrk 1486		NGC 2992 Sy2 nucl.	
Scenario	H II region winds		Lyman continuum escape		galaxy-scale outflows		AGN disk winds	
Feature(s)	H α , [N II] $\lambda\lambda 6548, 6583$		C II $\lambda 1334$		Si II $\lambda\lambda 1191, 1193$		[O III] $\lambda\lambda 4959, 5007$	
OutLines model	BetaCAK, PowerLaw, Sphere		BetaCAK, PowerLaw, Sphere, Launched		BetaCAK, DampedPulses, Sphere		AccPlaw, PowerLaw, HollowCones, Disk	
Parameters from MCMC Posterior Samples								
α	0.23 \pm	0.05	0.58 \pm	0.50			0.03 \pm	0.06
β	7 \pm	2	1.87 \pm	1.09	0.75 \pm	0.27	2.02 \pm	0.17
v_∞ [km s $^{-1}$]	309 \pm	14	195 \pm	17	567 \pm	42	925 \pm	65
b or σ_v [km s $^{-1}$]	30 \pm	0.5	5.0 \pm	2.4	64 \pm	20	82 \pm	1
Properties from MCMC Posterior Samples								
W_{50} (“FWHM”) [km s $^{-1}$]	47 \pm	1	88 \pm	4	184 \pm	27	235 \pm	28
W_{80} [km s $^{-1}$]	105 \pm	2	150 \pm	6	318 \pm	77	541 \pm	35
x_{out}	43 \pm	23	4.22 \pm	$\frac{11.83}{2.52}$	1.24 \pm	0.17	20 \pm	0.02
v_{out}	246 \pm	6	118 \pm	32	188 \pm	78	883 \pm	46
$\dot{M}/n_0 R_0^2$ [M_\odot yr $^{-1}$]	777 \pm	295	44.5 \pm	$\frac{268.0}{32.7}$	4.8 \pm	3.2	721 \pm	321
$\dot{p}/n_0 R_0^2$ [10^{34} dyne]	120 \pm	47	3.21 \pm	$\frac{27.00}{2.67}$	0.57 \pm	0.54	430 \pm	168
$\dot{E}/n_0 R_0^2$ [10^{42} erg s $^{-1}$]	15 \pm	6	0.19 \pm	$\frac{0.16}{2.09}$	0.05 \pm	0.05	195 \pm	70

from contamination such as stellar absorption except near permitted lines from, e.g., H I and He I. We subtract this continuum before modeling the line profile with OutLines with the default options. Then, we sample the posterior on the OutLines profile parameters to constrain the outflow and static gas properties. No LSF corrections are necessary as $R = 6000$ is sufficiently high to constrain the kinematics (see §3.2). We compare the best-fit model to the observed line profiles in Figure 17.

From the best-fit line fluxes, we determine the electron density of both the nebula and outflow components from the [S II] 6716/6731 flux ratio using PyNeb (Luridiana et al. 2015). The static gas flux ratio of 1.459 is in the low-density limit, requiring $n_e < 10 \text{ cm}^{-3}$. For the outflowing gas component, the doublet ratio is 0.831, which is where [S II] is most sensitive simultaneously to density and to temperature. For a range in T_e from 10 to 15 kK, the inferred outflow density is anywhere from 970 to 1140 cm^{-3} , with density values increasing with the assumed temperature. The implication from these densities is that the outflow is roughly two orders of magnitude more dense than the gas within the static nebular gas. While this increase in density may be due to a sweeping up of material in the wind, this dramatic change in density coupled with the supersonic flow implied by v_{out} could instead arise from compression by shocked gas as it rapidly cools via radiation (e.g., Flury et al. 2025a).

Though the posterior on β is not well constrained, the slope of the velocity field strongly favors $\beta > 4$, indicating gradual acceleration likely caused by optically thick radiation pressure from early type stars (e.g., Barlow & Cohen 1977). While Bresolin et al. (2020) argue that the non-thermal radio SEDs of Sramek & Weedman (1986) are clear-cut evidence for supernova-driven bubbles, the line profile shape indicates a continuous wind rather than shells or bubbles and, from modeling with OutLines, disfavors the supernova scenario. Indeed, the OutLines results are very much in agreement with the fact that Knot A features the a very young (< 3 Myr) cluster—in fact the youngest in the entirety of NGC 5471 (e.g., García-Benito et al. 2011, based on HST photometric color-magnitude diagrams). Knot A is also very massive ($> 10^4 M_\odot$) and requires a significant population of O stars to produce the $Q = 4 \times 10^{51}$ phot s $^{-1}$ associated with the star cluster (García-Benito et al. 2011). The age and mass of the stellar population indicate sufficient radiation available in the UV to radiatively drive a supersonic wind. Shocks triggered by this

wind could explain the non-thermal emission in the radio in addition to the dense gas. Inhomogeneities in the gas distribution can readily dissipate the outward force due to pressure from the hot shocked gas (e.g., Dyson 1977), allowing radiation pressure to dominate the acceleration of material out from the H II region. Our results indicating escape of hot gas are consistent with the Harper-Clark & Murray (2009) model for the Carina Nebula and the Lopez et al. (2011) multiwavelength study of the massive extragalactic H II region 30 Doradus, both of which found strong evidence for radiation pressure driving and a deficit of X-ray flux associated with shocked gas.

With the velocity field and line fluxes inferred by modeling nebular lines with OutLines, we have obtained key insight into the nature of the outflowing material: (i) that it is a wind, not a bubble, (ii) that the wind exhibits gas densities far higher than that of the static nebula, and (iii) that the wind is driven by substantial radiation pressure from O stars. These results are consistent with the observed stellar population ages. Moreover, this wind is supersonic, which could explain the non-thermal emission and high gas densities via shocks.

4.2 Lyman Continuum Escape from a Super Star Cluster

Starburst galaxy J1044+0353 is a low mass ($M_\star \approx 10^{6.8} M_\odot$) Lyman continuum emitter candidate with $f_{\text{esc}}^{\text{Lyc}}$ as high as 60% (Parker et al. 2025) and, as a nearby ($z = 0.01287$) Green Pea, is a local analog for star-forming galaxies at cosmic dawn that are actively involved in re-ionizing the Universe (Martin et al. 2024). Recent IFU observations of J1044+0353 reveal expanding shells of gas at the periphery of the nebular gas flux distribution (Martin et al. 2024), indicative of blowout due to SNe from an aging stellar population 10–20 Myr after a burst of star formation (Peng et al. 2023). However, the central core of the galaxy hosts a super star cluster with several young (< 2 Myr) stellar populations which may be responsible for driving additional feedback on shorter timescales (Olivier et al. 2022), providing a unique laboratory to explore the impact of young stars on their immediate environment in the context of stochastic, or bursty, star formation using OutLines.

To undertake this investigation, we draw on archival HST/COS G130M FUV spectroscopy ($R = 10\,000$) of the central starburst of J1044+0353 from the COS LegAcy Spectroscopic Survey (CLASSY, Berg et al. 2022; James et al. 2022, GO 15840), which

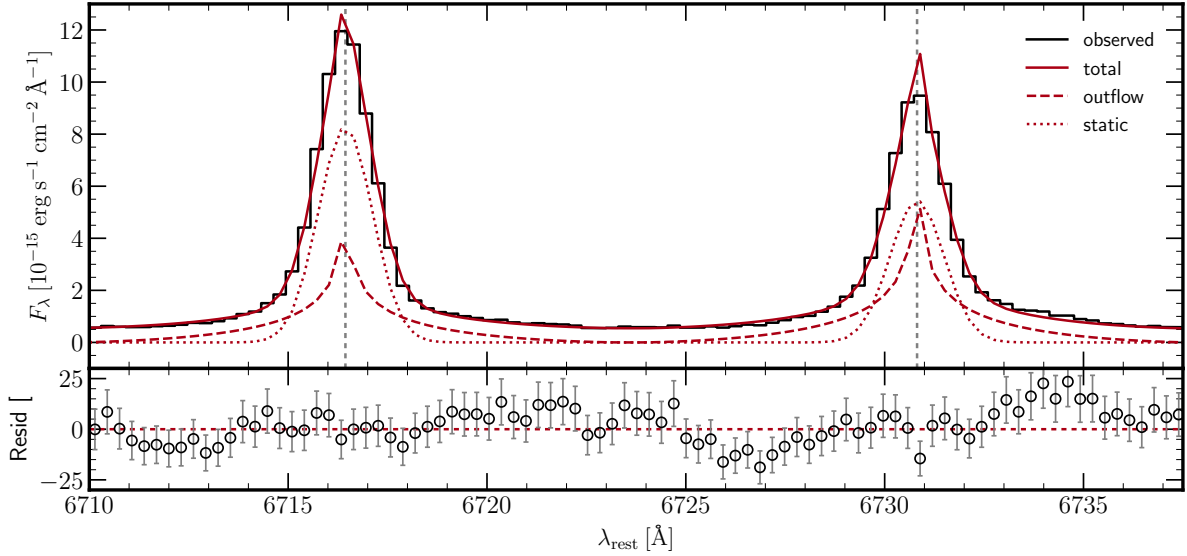


Figure 17. *Top:* [S II] $\lambda\lambda 6716, 6731$ doublet in Knot A of NGC 5471. Grey dashed vertical line indicates the line center given by atomic data. The best-fit OutLines.Nebular model is shown in red with the outflow (dashes), static (dotted), and total (solid) line profiles. *Bottom:* residual difference between the best-fit OutLines profile and the observed spectrum.

allows for detailed modeling of outflow properties along the line of sight without significant effects from the LSF even after downsampling to the 0.073 \AA resolution (see Berg et al. 2022; James et al. 2022; Parker et al. 2024). The C II $\lambda 1334$ absorption line is one of the strongest low ionization lines in the FUV due to the transition oscillator strength and comparatively high ionic abundance, making it an excellent tracer of outflows. Visual inspection of the C II line profile suggests a classic blue-shifted continuous outflow plus a static ISM component (see, e.g., Figure 1 of Heckman et al. 2015). To obtain the normalized flux, we fit the starlight continuum within 3 \AA of the feature with a third-order polynomial and divide the local spectrum by this fit (see, e.g., the VoigtFit software, Krogager 2018, which takes a similar approach using Chebyshev polynomials).

For modeling the C II line with OutLines, we use atomic data from Morton (2003). No infilling is apparent in the observed line profile, suggesting either maximal aperture clipping where pure absorption is an appropriate description of the emergent feature (see Figure 8) or an optically thick wind. For simplicity, we assume the OutLines default geometry and density profile, although we note that applying more sophisticated geometry or density profiles negligibly impacts the quality of the fit. Indeed, a filled cone model yields best-fit inclinations of $i \rightarrow 0^\circ$ and opening angles of $\theta_o \rightarrow 90^\circ$, consistent with the filled sphere geometry. Additional consideration of pulse-like density profiles consistently favors a peak location at the base of the outflow with wide dispersion, which combined are consistent with the power law approximation. However, the sudden drop in flux immediately blueward of the systemic velocity of the system suggests a non-zero launch velocity. We therefore allow for non-zero launch velocities. The OutLines default top hat (uniform-bounded) prior is assumed. Best-fit parameters are in Table 1.

While the COS G130M grating resolution is in the LSF-insensitive regime, COS LSFs contain prominent broad non-Gaussian wings which necessitate folding in LSF corrections. As such, we perform our fit a second time by convolving the OutLines profile with the appropriate COS G130M LSF (see <https://www.stsci.edu/hst/instrumentation/cos/performance/spectral->

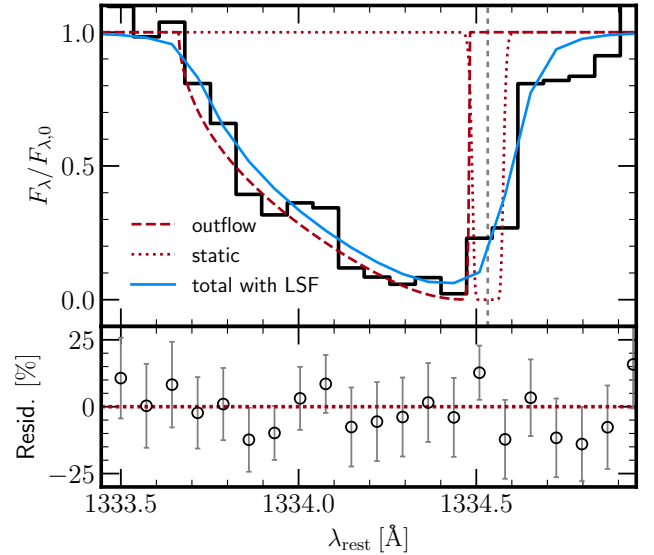


Figure 18. MCMC fit of an OutLines.Absorption model to the C II $\lambda 1334$ absorption line observed by *HST*/COS G130M (black, Berg et al. 2022). Line styles and colors as in Figure 17. Blue line indicates the intrinsic profile convolved with the *HST*/COS G130M line spread function (LSF).

resolution and method in Appendix B of Flury et al. 2025b) before comparing it to the observations. We find that the results from our initial fit are comparable to those from the fit containing the LSF correction, with each set of parameters well within the 1σ confidences of both posteriors.

The best-fit parameters indicate that the starbursting core of J1044+0353 contains a spherical expanding wind with a velocity field characteristic of radiatively-driven winds most likely due to dusty radiation pressure (e.g., Flury et al. 2023), although line-driving (Castor et al. 1975a) and optically thick (Barlow & Cohen

1977) mechanisms are consistent with the range of β . Critically, the posterior on β strongly disfavors ram pressure driving, suggesting that supernovae do not cause the current feedback. However, the relatively low wind velocity ($v_\infty = 215 \text{ km s}^{-1}$, comparable to Voigt modeling of the silicon lines, [Parker et al. 2024](#), and the “broad” component of nebular lines, [Peng et al. 2023](#)) and weak \dot{p} and \dot{E} (marginally non-zero) suggests that mechanical feedback from massive stars is relatively weak or even suppressed. Such suppression can occur in cases where catastrophic cooling of swept up dense material prevents acceleration up to more “traditional” velocities closer to 500 km s^{-1} or more, is known to occur in Green Pea galaxies with young stellar populations ([Jaskot et al. 2017](#)), and could be associated with Lyman continuum (LyC) escape (e.g., [Jaskot et al. 2017, 2019](#)). Combined with evidence for recent SNe, the weak feedback inferred from `OutLines` models supports the bursty star formation scenario for LyC escape suggested by [Flury et al. \(2022\)](#) in their assessment of a large sample of star-forming galaxies with LyC detections and later demonstrated by [Flury et al. \(2025b\)](#) with measurement of stellar populations and ISM conditions in stacks of UV spectra of LyC emitters. In their framework, SNe clear out channels in the ISM via mechanical feedback and a subsequent generation of stars 8-10 Myr later provides ionizing—but not mechanical—feedback to establish the density-bounded conditions necessary for Lyman continuum photons to escape anisotropically. Here, inferring underlying physics and wind properties from a single-aperture spectrum demonstrates the power and effectiveness of `OutLines` in understanding the role of mechanical feedback in LyC escape.

4.3 Outflow Formation and Blowout in a Starburst Galaxy

Mrk 1486 is a starburst galaxy exhibiting a tentative He II $\lambda 4686$ Wolf-Rayet feature (e.g., [Izotov et al. 1997](#)), metal rich extraplanar biconical outflows beyond the galactic plane (e.g., [Duval et al. 2016; Cameron et al. 2021](#)), and > 14 Myr stellar populations ([Parker et al. 2025](#), although see [Peng et al. 2025](#), who find from the same UV spectra that these populations are even older, ≈ 100 Myr). The archival *HST*/COS spectrum from [Rivera-Thorsen et al. \(2015, GO 12583, PI Hayes\)](#) exhibits the classic blue-shifted asymmetric feature associated with outflows, albeit with at least two troughs present in the outflow feature across several low ionization lines (Si II $\lambda\lambda 1191, 1193, 1304$, O I $\lambda 1302$, and Al II $\lambda 1670$, see [Rivera-Thorsen et al. 2015](#) their Figure 3, [Parker et al. 2024](#), their Figure 7). A multi-troughed absorption feature can indicate an ensemble of shells produced by a series of episodes or a system of many star clusters (see Figure 5, also [Rivera-Thorsen et al. 2015](#)).

For our analysis, we use the [Rivera-Thorsen et al. \(2015\)](#) spectrum reprocessed by [Berg et al. \(2022\); James et al. \(2022\)](#), down-sampled to 0.073 \AA resolution and normalized following the polynomial approach in §4.2. To determine the origin of this multi-episode outflow, we can use `OutLines` to model the absorption lines. The Si II $\lambda\lambda 1191, 1193$ doublet provides an excellent probe as both features arise from the same ion, thus providing additional constraining power. The stronger Si II $\lambda 1260$ line is contaminated by telluric O I $\lambda 1302$ and cannot be used to constrain the fit. We note the presence of weak Si II $\lambda 1194, 1197$ fluorescent emission arising from the re-emission of Si II $\lambda\lambda 1191, 1193$ photon absorption, respectively. These lines suffer from apparent Milky Way contamination in the blue wings due to absorption by Galactic O IV $\lambda\lambda 1234, 1237$, Si III $\lambda 1235$, and Mn II $\lambda\lambda 1234, 1236$. We mask these features in order to include the fluorescent lines in our fit. Using atomic data from [Kelleher & Podobedova \(2008\)](#) obtained from NIST ([Kramida et al. 2024](#)) and the appropriate COS G130M LSF, we model the Si II

doublet complex of $\lambda\lambda 1191, 1193$ resonant absorption and emission and $\lambda\lambda 1194, 1197$ fluorescent emission using `OutLines` assuming a damped-pulses density profile to account for the multiple absorption troughs and otherwise adopting the default options of a spherical geometry and the β CAK velocity field. The choice of spherical geometry is supported by the presence of relatively symmetric fluorescent Si II $\lambda\lambda 1194, 1197$ lines, although the COS LSF may complicate any inference of the geometry. As in §4.2, we incorporate the appropriate LSF corrections.

The two Si II absorption lines have similar depths. Given the oscillator strengths of the two transitions, the Si II $\lambda 1193$ line should be deeper than Si II $\lambda 1191$. For the lines to have similar depths, the Si II $\lambda 1193$ line must be saturated. Whether the Si II $\lambda 1191$ line is saturated is not ascertainable solely from the relative line depths; however, the prominent $\lambda\lambda 1194, 1197$ lines suggest optically thick lines consistent with trapping of the resonant emission, with many scattering events allowing photon escape solely through fluorescent channels, i.e., no resonant emission. Because $\lambda 1193$ is saturated and has a depth similar to that of $\lambda 1193$ (minimal infilling by the $\lambda 1194$ line), any transmitted flux must be due to starlight within the spectroscopic aperture that is not associated with the foreground gas. Traditionally, such residual flux is explained by a partial gas covering fraction, with the radiative transfer rewritten as

$$\frac{F_\lambda}{F_{\lambda 0}} = 1 - C_f [1 - \exp(-\tau_0 \phi_\lambda)] \quad (44)$$

where C_f expresses the fraction of background light which is not obstructed by the foreground gas (e.g., [Netzer 1982; Arav et al. 1999, 2005; Rivera-Thorsen et al. 2015](#)). The COS LSF can affect the partial covering fractions of saturated absorption lines (see, e.g., assessment by [Flury et al. 2025b](#), their Appendix D, also Figure 3 of [Jennings et al. 2025](#)). Incorporating both C_f and ϵ as free parameters into the initial fit, we find that while the COS LSF and infilling by the 1194 fluorescent line can account for some of the line profile depths, $C_f = 0.82 \pm 0.03$ is necessary to provide an optimal description to the absorption features (comparable to the $C_f = 0.8$ obtained by [Rivera-Thorsen et al. 2015](#)). We also find $\epsilon = 0.21 \pm 0.03$ necessary to describe the fluorescent line profile.

We show the best-fit line profile in Figure 19 and list the results in Table 1. As a test of our assumption of spherical geometry, we predict the emergent fluorescent Si II $\lambda\lambda 1194, 1197$ lines using `OutLines.Fluorescent` and the best-fit parameters from the posterior, which we show in Figure 19.

The posterior sampling indicates relatively small uncertainties on the order of 10% for each of the expanding shells, with the most prominent and lowest velocity shell having $v_{\text{shell}} = 188 \pm 20 \text{ km s}^{-1}$ (obtained from $v_{\text{shell}} = v_\infty w[x_1]$ and propagating the uncertainties in x_1, β , and v_∞). The system of shells suggest an outflow in formation, with regular events forming thin expanding superbubbles. Notably, the less pronounced absorption troughs in C II $\lambda 1334$, which traces a higher ionization state than Si II, O I, and Al II, suggests that the ionized phase of the outflow is established more rapidly than the neutral phase and may indicate that the expanding bubbles are entrained in or even driven by a hotter phase of the ISM. The accumulation of superbubbles close to the terminal velocity suggests that an outflow forms from these successive events with sufficient speed to exceed the escape velocity ($v_{\text{esc}} \approx 100 \text{ km s}^{-1}$ as implied by the $M_\star = 10^{9.3} M_\odot$ from [Chisholm et al. 2018](#)). The recurrence of many such expanding shells could produce the biconical outflow observed in emission once the superbubbles escape the gravitational potential and blow out from the galactic disk (see spatially resolved cases in, e.g., [Martin 1998; McQuinn et al. 2019, and Duval et al. 2016](#) specifically regarding

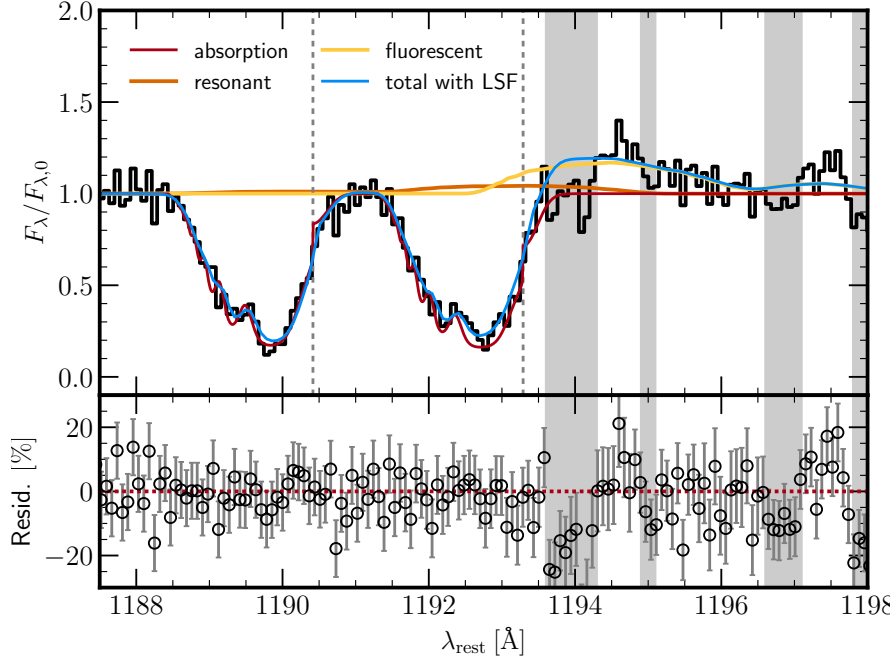


Figure 19. MCMC fit of an OutLines model to the Si II $\lambda\lambda 1191, 1193, 1194, 1997$ doublet complex observed by *HST*/COS G130M (black, [Rivera-Thorsen et al. 2015](#), GO 12583, PI Hayes). Shaded regions indicate suspected Milkyway contamination from Galactic Si III, Mn II, and O IV. Si II $\lambda\lambda 1191, 1193$ resonant emission lines computed using OutLines. Resonant are shown in orange, demonstrating strong radiative trapping. Si II $\lambda\lambda 1194, 1197$ fluorescent lines computed using OutLines. Fluorescent are shown in yellow. Total line profile corrected for the line spread function (LSF) is shown in blue. Other line styles, symbols, and colors as in Figure 17.

Mrk 1486). Moreover, the successive events are removing gas at mass outflow rates of $\dot{M} = 4.8 M_{\odot} \text{ yr}^{-1}$, which may temporarily rob the galaxy of baryonic material necessary to sustain the production of stars and could explain the 30-40 Myr lapse between bursts of star formation.

Given that the outflows in Mrk 1486 are oxygen rich relative to their host galaxy ([Cameron et al. 2021](#)), it is useful to consider whether the outflow component of Si II is metal-enhanced since, like oxygen, silicon is an α element and is predominantly produced by core-collapse supernovae (CCSNe, e.g., [Kobayashi et al. 2020](#)). From the best-fit line profiles from OutLines, the outflow $N_{\text{O Si}^+} = 10^{15.5} \text{ cm}^{-2}$ while the static $N_{\text{S Si}^+} = 10^{13.5} \text{ cm}^{-2}$. Ionization structure may account for some of the difference in Si⁺; nevertheless, the 2 dex increase in the outflow likely suggests substantial metal loading of the outflow (see, e.g., [Chisholm et al. 2018](#)) due to enrichment by recent CCSNe.

It may be tempting to conclude that hot gas or cosmic rays from these supernovae are driving the shells' expansion, especially since, for the lowest velocity shell at 188 km s^{-1} , the dynamical time to traverse the inner 500 pc is $\lesssim 2.5 \text{ Myr}$, well after the onset of CCSNe for a burst at least 10 Myr old. That being said, the age reported by [Parker et al. \(2025\)](#) from fits to the UV continuum that Mrk 1486 corresponds to a combination of a substantial young ($\leq 5 \text{ Myr}$) stellar population and a far older (40 Myr) population. In light of the more detailed star formation history, while CCSNe may be the progenitors of the material in these expanding shells, they may not necessarily be responsible for their acceleration. Here, the shape of the velocity field from OutLines can provide insight into the driving mechanism. Indeed, the velocity index of $\beta = 0.7 \pm 0.2$ disfavors (but cannot fully not reject) the rapid acceleration associated with ram pressure driving ($\beta \lesssim 0.5$, e.g., [Murray et al. 2005](#); [Chisholm et al. 2016](#)). However, these α -rich shells are more likely continuously

accelerated by optically thin line-driven radiation pressure associated with $\beta = 0.8$ (e.g., [Pauldrach et al. 1986](#)). Moreover, the total energy injection rate of $10^{40} \text{ erg s}^{-1}$ for the series of shells is roughly consistent with stellar winds, which have $L_{\text{mech}} \approx 10^{39} \text{ erg s}^{-1}$ for a given stellar population (see, e.g., [Starburst99](#) or [BPASS](#), [Leitherer et al. 2014](#); [Byrne et al. 2022](#), respectively). Radiative driving by young stellar populations may also account for the less pronounced C II troughs via ionizing feedback. Furthermore, given that the travel time from the nucleus to a 1 kpc radius (roughly the COS aperture at the 139.1 Mpc distance of Mrk 1486) is $\lesssim 5 \text{ Myr}$, the $> 40 \text{ Myr}$ stellar populations are unlikely to be responsible for these superbubbles. Corroborating evidence for optically thick radiation pressure is the presence of the fluorescent $\lambda\lambda 1194, 1197$ lines but the absence of resonant line infilling. Such a scenario occurs in the optically thick line limit where photon escape primarily occurs through the fluorescent channel (e.g., [Scarlata & Panagia 2015](#), their Figures 5-6).

The bursty star formation in Mrk 1486 could optimize the production of α elements and energetic expanding shells via CCSNe from earlier generations of stars while the most recent stellar populations provide the momentum injection via radiation pressure to form and accelerate optically thick enriched superbubbles, driving them beyond the galactic disk to form an outflow. OutLines is necessary here to infer the velocities of the shells as they accelerate under a collective driving mechanism, determine the relative importance of SNe and young stars in producing and accelerating these shells, and whether the shells are capable of eventually exceeding the escape velocity to form an outflow.

4.4 Thermal Winds in AGN Radio Lobes

The Seyfert 2 galaxy NGC 2992 has long been known to exhibit conical outflows (Allen et al. 1999; Veilleux et al. 2001). Using archival observations from the Siding Spring Seyfert Spectroscopic Snapshot Survey (S7, Thomas et al. 2017) made using WiFES (Dopita et al. 2010), we have confirmed broad, asymmetric [O III] $\lambda\lambda 4959, 5007$ lines after summing over all the spaxels to boost signal to noise in the line profile and to mitigate any aperture effects. The low resolution ($R \approx 3\,000$ or FWHM of 105 km s^{-1}) requires corrections for the LSF by convolving with a Gaussian kernel with $\sigma_{\text{LSF}} = 45\text{ km s}^{-1}$; however, we note that the LSF predominantly impacts the narrow Gaussian core. The high signal in the wings ($S/N \approx 3$ in the blue broad extent of [O III] $\lambda 4959$) might allow for tight constraints on the wind properties even without LSF corrections – indeed fitting with and without LSF corrections yields similar results for the OutLines parameters. Nevertheless, incorporating the LSF into the forward modeling with OutLines is essential to remain consistent with the observations. As a part of the LSF correction, we fold in the summed best-fit stellar continuum included in S7 to account for stellar contributions to the continuum, including any contamination of the line profile.

The bright intermediate portion of the wings suggests the acceleration power law for the velocity field. Visual assessment of the highly asymmetric line profile in the spectrum of NGC 2992 and comparison with models in Figures 11, 12, and 14 also suggests a hollow cone geometry with an obstructing disk. As such, we subsequently model the [O III] doublet using OutLines assuming an acceleration power law, an open cone geometry, and an obstructing disk. We impose the following into the prior: line fluxes within 5% of the [O III] 5007/4959 flux ratio of 2.98 given by atomic data (Storey & Zeippen 2000) and $\theta_o - \theta_c > 5^\circ$. With line profiles predicted by OutLines added to the continuum and subsequently convolved with the WiFES LSF (Dopita et al. 2010), we use emcee to sample the posterior on the outflow parameters. Due to the large number of parameters, potential degeneracies, and sensitivity to initial conditions, we run the sampler four times longer, for a total of 40 000 samples post burn-in. Implementation of our modeling is demonstrated for reference in Appendix C with the best-fit profile shown in Figure 20 and results listed in Table 1. We note that the posterior sampling ultimately rejects the priors on the angles as the best-guess parameters fell within a local minimum.

From the posterior on the profile parameters, we find terminal velocities in excess of $1\,000\text{ km s}^{-1}$, indicative of a strong outflow. While this value is far greater than those previously reported for this object, the full width at half flux (FWHF) given by the 25-75 percentiles is km s^{-1} , consistent with the flux-weighted average found by Veilleux et al. (2001). Additionally, Allen et al. (1999) suggest that velocities closer to 500 km s^{-1} are necessary to account for possible shock excitation of gas in the outflow. The $v_{\text{out}} = 596\text{ km s}^{-1}$ from the best-fit OutLines profile could readily provide the conditions necessary for such shock excitation.

The slope $\beta = 2.02$ indicates, for the acceleration power law velocity field, rapid acceleration to the terminal velocity (see Figure 2), which can be interpreted as thermal (ram pressure) or cosmic ray (magnetic pressure) driving as each can produce similar rapid-acceleration velocity fields based on the shape of the velocity field (see Figure 1, also Murray et al. 2005; Chisholm et al. 2016; Flury et al. 2023). Thermal driving occurs when “cool” (10^4 K) clouds are embedded in an adiabatically expanding hot ($> 10^6\text{ K}$) gas (Murray et al. 2005). Cosmic ray occurs driving where clouds are accelerated by the diffusion (Breitschwerdt et al. 1993; Quataert et al. 2022b) or

streaming (Ipavich 1975; Breitschwerdt et al. 1991; Quataert et al. 2022a) of relativistic charged particles—launched by hot ionized media such as shocks or supernovae (Colgate & Petschek 1979; Blandford & Ostriker 1980)—as they interact with magnetic fields in the ISM, resulting in a radially outward pressure gradient. NGC 2992 is known to contain $\approx 0.5\text{ kpc}$ radio lobes forming an hourglass or “figure eight” shape, indicative of bi-directional bubbles of hot gas driven by nuclear activity (Wehrle & Morris 1988; Allen et al. 1999). Combining optical and radio measurements indicates the presence of hot cavities which are heated (likely through shocks) by jets or accretion disk winds and within which are entrained clouds of cooler gas (Allen et al. 1999; Veilleux et al. 2001). The presence of such lobes and the associated hollow cavities suggests either or both (a plausible scenario, e.g., Breitschwerdt et al. 2002; Everett et al. 2008) mechanisms are involved in launching the outflow in NGC 2992.

Spatial analysis of the outflow in Veilleux et al. (2001) found an inclination of $i = 68 \pm 3^\circ$ and an opening angle of $\theta_o = 62.5 - 67.5^\circ$. OutLines finds $i = 53.19 \pm 1.32^\circ$ and $\theta_o = 68.60 \pm 1.26^\circ$. While θ_o is in apparent agreement, i is significantly discrepant, requiring further assessment of the fit results. To test the reliability of the geometry inferred from the OutLines model, we project the best-fit bidirectional cones onto the plane of the sky and compare with the spatially resolved continuum-subtracted [O III] doublet flux in the WiFES IFU in Figure 21. We find good agreement between the cone geometry implied by the integrated line profile using OutLines and the observed flux distribution, indicating that modeling with OutLines can recover the spatial geometry without any knowledge of that geometry a priori. Not only have we accurately recovered the spatial flux distribution with OutLines, but we have also inferred the presence of a cavity comprising the inner two thirds of the outflow cone ($\theta_c = 48.64 \pm 1.82^\circ$), suggesting that cooler line-emitting clouds can only survive towards the edges of the hot cavity where the thermal wind may be somewhat cooler as it expands and contacts the surrounding ISM.

With the best-fit parameters, OutLines computes high mass loss rates of at least $40\text{ M}_\odot\text{ yr}^{-1}$. From the $v_0 \sim 300\text{ km s}^{-1}$ rotational velocity of the galaxy (Veilleux et al. 2001), the outflow must be capable of ejecting material from the host galaxy with the characteristic velocity exceeding the escape velocity by a factor of 3. Together, these results suggest NGC 2992 is in a state of AGN-triggered inside-out quenching with the combined effects of hot cavities and the evacuation of cool gas away from the plane of the galaxy, both effects preventing future star formation. Interestingly, this quenching feedback is not sufficiently columnated to be driven by a jet but instead is most likely due to expanding gas heated by winds launched from the accretion disk. While the implications of quenching are clear for galaxy evolution, the association of hot winds and shocks also has implications for the measurement of chemical abundances in AGN (e.g., Dors et al. 2021). Here, inferring underlying physics, geometry, and outflow strength from a single-aperture spectrum demonstrates the power and effectiveness of OutLines in the context of AGN feedback.

5 CONCLUSION

Here, we present a novel method for modeling emission and absorption lines arising from astrophysical winds, bubbles, and outflows. Our method has many advantages over previous methods, such as multi-Gaussian and Gauss-Hermite models or velocity quantiles, in that it is physically motivated but also agnostic to underlying conditions or assumptions about the driving mechanism(s). Moreover,

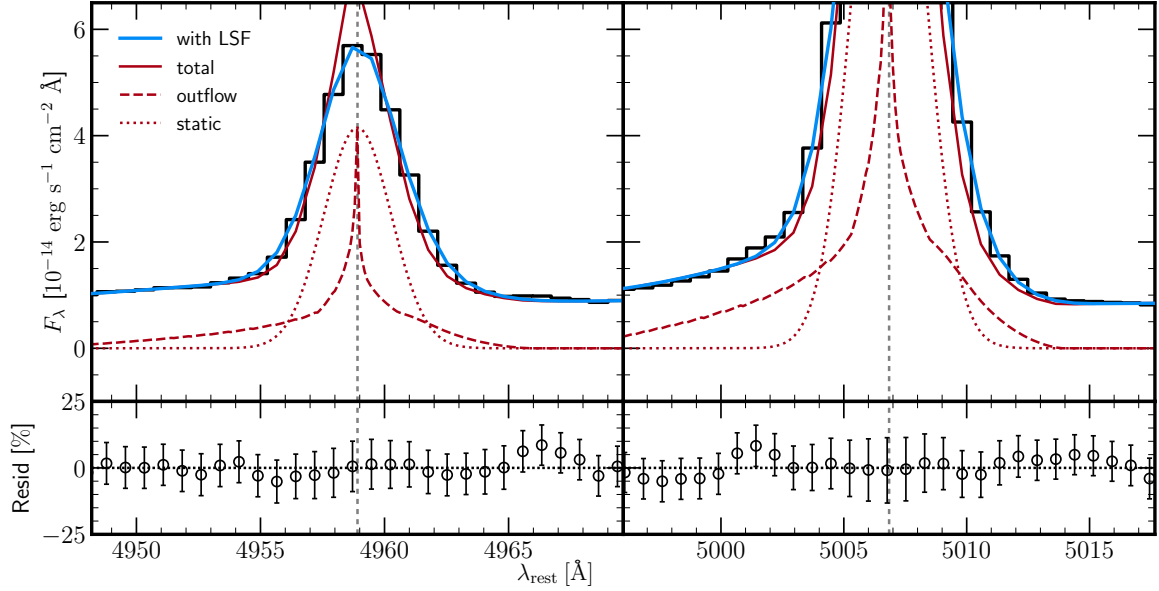


Figure 20. MCMC fit of an `OutLines.Nebular` model to the $[\text{O III}] \lambda\lambda 4959, 5007$ doublet observed in the nucleus of Seyfert galaxy NGC 2992 as part of the Siding Spring Seyfert Spectroscopic Snapshot Survey (S7, Thomas et al. 2017) DR2, assuming a hollow cone plus disk outflow geometry. Line styles and colors as in Figure 17. Blue line indicates the profile after LSF correction.

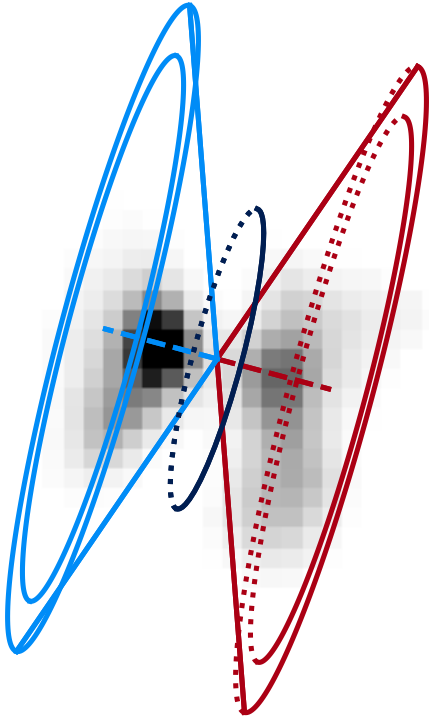


Figure 21. Greyscale map across the central kiloparsec of NGC 2992 of the continuum-subtracted, integrated $[\text{O III}]$ doublet flux in the S7 DR2 (Thomas et al. 2017). Drawn cones indicate the geometry inferred from the best-fit `OutLines` profile to the *integrated* emission line profile. No spatial information was used to determine the shape of the projected cones. Blue indicates the anterior cone, red indicates the posterior cone. Indigo indicates the disk, here with arbitrary radius scaled for visualization. A PA of 75° was assumed to rotate the projected geometry to the PA of the observation.

our model is readily applicable to absorption and emission line profiles. Improvements over a previous implementation of this method include i) multiple approximations to the velocity field from the wind equations of motion: a velocity power law, an acceleration power law, and the CAK theory β law; ii) a variety of density profiles expressing continuous (power law, double power law exponential) and single-episode (normal, log normal, fast-rise exponential decay) scenarios as well as a composite of many expanding shells or bubbles and iii) different geometries (spherical, filled cones, and hollow cones, with cones accompanied by an optional disk). All these scenarios are consistent with conditions observed in stars, nebulae, and galaxies.

We have made this modeling approach publicly accessible through the open-source software `OutLines` in `python`, available via `pip` and `GitHub` facilities. To date, `OutLines` is the only line profile code with such extensive and interchangeable geometries, density profiles, and velocity fields, making it by far the most comprehensive and versatile tool available for the study of outflows, winds, and bubbles. We illustrate the usefulness of the `OutLines` software with application to an H II region, a super star cluster, a starburst galaxy, and an AGN, deriving properties based on the line profile models. Furthermore, we demonstrate how the results from modeling with `OutLines` provide insight into the underlying physics of winds, bubbles, and outflows, obtaining the following results specifically made possible through our custom line profiles:

- Young (< 4 Myr) H II regions undergoing expansion can exhibit two orders of magnitude in gas compression due to wind-triggered shocks even while optically thick radiation pressure is the main driving mechanism of the bulk motion of the gas. Thus, while shocks may dominate the radio continuum, it is radiation pressure from stars which primarily shapes the evolution of young H II regions.
- Suppression of optically thin radiative feedback occurs in young (< 2 Myr) super star clusters in dwarf galaxies like the Green Peas indicates that the most recent stellar populations cannot mechanically evacuate optically thin channels for Lyman continuum photons to escape. Mechanical feedback from previous episodes of star formation

may be necessary to shape the gas geometry for subsequent populations to leak ionizing radiation. Thus it is ionizing feedback from the most recent stellar populations which produces the density-bounded conditions in low gas density channels through which Lyman continuum photons escape.

- Expanding superbubbles produced by core-collapse supernovae can, in succession, accumulate up to produce an outflow as the shells relax or dissipate into a more continuous flow; however, optically thick radiation pressure is necessary for these shells to accelerate to the terminal velocity before blowout and formation of bidirectional cones extended beyond the galactic disk. The formation of outflows from systems of metal-rich shells indicates that radiative driving is a key mechanism in the baryon cycle which shapes the scaling relations of galaxies across cosmic time.
- Accretion disk winds of a Seyfert galaxy are sufficiently fast to trigger substantial shocks in the central kiloparsec. The resulting hot fluid drives an outflow via pressure generated from the hot gas itself or from cosmic rays accelerated by the shock. The outflow consists of “cold” clouds entrained in the periphery of hollow cones and has the potential to cause inside-out quenching as it impacts the host galaxy.

This broad applicability and deep insight into the physics of outwardly moving gas demonstrates that *OutLines* is powerful tool which will prove to be useful across the astronomical community. Future work will involve application to massively multiplexed fiber spectroscopic surveys like WEAVE-LOFAR and 4MOST/WAVES for statistical assessments and to hydrodynamical simulations to explore the underlying physics.

ACKNOWLEDGEMENTS

We thank the beta testers, including K. Z. Arellano Cordova, K. Duncan, A. Hall, and T. Horn, whose efforts helped to optimize the use of this code. We thank K. Z. Arellano Cordova, C. Esteban, and J. Garcia-Rojas for providing access to Knot A extractions from their reduced MEGARA data. We thank K. Parker for sharing results from the recently accepted [Parker et al. \(2025\)](#). We thank K. Duncan for insight and comments regarding this manuscript. We thank A. Rankine and A. Lawrence for suggestions regarding the relativistic corrections. We also thank M. Divakara and G. Romero-Cruz for insightful discussions about outflow geometry at the National Institute of Astrophysics, Optics and Electronics (INAOE) and J. Chisholm, C. Martin, and N. Murray for insightful discussions about winds, massive stars, feedback, and *HST*/COS at the Aspen Center for Physics.

This work was performed in part at the Aspen Center for Physics, which is supported by a grant from the Simons Foundation (1161654, Troyer) and by National Science Foundation grant PHY-2210452.

Support for *HST* GO programs 12583 and 15840 was provided by NASA through a grant from the STScI, which is operated by the Association of Universities for Research in Astronomy, Inc., under NASA contract NAS 5–26555.

Facilities: *HST*, *GTC*, *SSO*

Software, repositories, and other digital resources: *corner* ([Foreman-Mackey 2016](#)), *curlyBrace*, *emcee* ([Foreman-Mackey et al. 2013](#)), *matplotlib* ([Hunter 2007](#)), *MAST*, *NIST/ASD* ([Kramida et al. 2024](#)), *numpy* ([van der Walt et al. 2011](#)), *OutLines* (this work, see also [10.5281/zenodo.11238265](#)), *PyNeb* ([Luridiana et al. 2015](#)), *S7 DR2* ([Thomas et al. 2017](#)), *scipy* ([P. Virtanen 2020](#)), *vygrboi*

AI use: No language learning model or otherwise generative artificial intelligence was used in this work.

DATA AVAILABILITY

The data underlying this article for NGC 5471 were provided by K. Z. Arellano Cordova, C. Esteban, and J. Garcia-Rojas by permission. Data will be shared on reasonable request to the corresponding author with permission of the above owners. The data underlying this article for J1044+4012 and Mrk 1486 are publicly available from *MAST*. The data underlying this article for NGC 2992 are publicly available from *S7 DR2*.

The *OutLines* code presented here is publicly available on github.com/sflury/OutLines under DOI [10.5281/zenodo.11238265](https://doi.org/10.5281/zenodo.11238265) or from *PyPI* via `pip install SpecOutLines`.

REFERENCES

- Abbott D. C., 1977, PhD thesis, University of Colorado, Boulder
- Allen M. G., Dopita M. A., Tsvetanov Z. I., Sutherland R. S., 1999, *ApJ*, **511**, 686
- Arav N., Becker R. H., Laurent-Muehleisen S. A., Gregg M. D., White R. L., Brotherton M. S., de Kool M., 1999, *ApJ*, **524**, 566
- Arav N., Kaastra J., Kriss G. A., Korista K. T., Gabel J., Proga D., 2005, *ApJ*, **620**, 665
- Axon D. J., Taylor K., 1978, *Nature*, **274**, 37
- Bae H.-J., Woo J.-H., 2016, *ApJ*, **828**, 97
- Barlow M. J., Cohen M., 1977, *ApJ*, **213**, 737
- Beals C. S., 1931, *MNRAS*, **91**, 966
- Berg D. A., et al., 2022, *ApJS*, **261**, 31
- Berger E., Zauderer A., Pooley G. G., Soderberg A. M., Sari R., Brunthaler A., Bietenholz M. F., 2012, *ApJ*, **748**, 36
- Bianchi S., et al., 2026, arXiv e-prints, p. [arXiv:2602.16252](https://arxiv.org/abs/2602.16252)
- Binette L., Drissen L., Ubeda L., Raga A. C., Robert C., Krongold Y., 2009, *A&A*, **500**, 817
- Blandford R. D., Ostriker J. P., 1980, *ApJ*, **237**, 793
- Breitschwerdt D., McKenzie J. F., Voelk H. J., 1991, *A&A*, **245**, 79
- Breitschwerdt D., McKenzie J. F., Voelk H. J., 1993, *A&A*, **269**, 54
- Breitschwerdt D., Dogiel V. A., Völk H. J., 2002, *A&A*, **385**, 216
- Bresolin F., et al., 2020, *MNRAS*, **495**, 4347
- Byrne C. M., Stanway E. R., Eldridge J. J., McSwiney L., Townsend O. T., 2022, *MNRAS*, **512**, 5329
- Cameron A. J., et al., 2021, *ApJ*, **918**, L16
- Carr C., Scarlata C., Panagia N., Henry A., 2018, *ApJ*, **860**, 143
- Castor J. I., 1970, *MNRAS*, **149**, 111
- Castor J. I., Lamers H. J. G. L. M., 1979, *ApJS*, **39**, 481
- Castor J. I., Abbott D. C., Klein R. I., 1975a, *ApJ*, **195**, 157
- Castor J., McCray R., Weaver R., 1975b, *ApJ*, **200**, L107
- Chevalier R. A., Clegg A. W., 1985, *Nature*, **317**, 44
- Chisholm J., Tremonti Christy A., Leitherer C., Chen Y., 2016, *MNRAS*, **463**, 541
- Chisholm J., Tremonti C., Leitherer C., 2018, *MNRAS*, **481**, 1690
- Chu Y.-H., Kennicutt Jr. R. C., 1986, *ApJ*, **311**, 85
- Chu Y.-H., Kennicutt Jr. R. C., 1994, *ApJ*, **425**, 720
- Clegg R. E. S., Harrington J. P., Barlow M. J., Walsh J. R., 1987, *ApJ*, **314**, 551
- Colgate S. A., Petschek A. G., 1979, *ApJ*, **229**, 682
- Colina L., Lipari S., Macchetto F., 1991, *ApJ*, **379**, 113
- Crenshaw D. M., Kraemer S. B., 2000, *ApJ*, **532**, L101
- Crenshaw D. M., Kraemer S. B., 2012, *ApJ*, **753**, 75
- Crenshaw D. M., et al., 2000, *AJ*, **120**, 1731
- Cronin S. A., et al., 2025, arXiv e-prints, p. [arXiv:2505.04707](https://arxiv.org/abs/2505.04707)
- Das V., Crenshaw D. M., Kraemer S. B., Deo R. P., 2006, *AJ*, **132**, 620
- Dopita M. A., et al., 2005, *ApJ*, **619**, 755
- Dopita M., et al., 2010, *Ap&SS*, **327**, 245
- Dors O. L., Contini M., Riffel R. A., Pérez-Montero E., Krabbe A. C., Cardaci M. V., Hägele G. F., 2021, *MNRAS*, **501**, 1370
- Duval F., et al., 2016, *A&A*, **587**, A77
- Dyson J. E., 1977, *A&A*, **59**, 161

- Dyson J. E., 1979, *A&A*, **73**, 132
- Einstein A., 1905, *Annalen der Physik*, **322**, 891
- Eldridge J. J., Stanway E. R., Xiao L., McClelland L. A. S., Taylor G., Ng M., Greis S. M. L., Bray J. C., 2017, *Publ. Astron. Soc. Australia*, **34**, e058
- Esteban C., Peimbert M., 1995, *A&A*, **300**, 78
- Everett J. E., Zweibel E. G., Benjamin R. A., McCammon D., Rocks L., Gallagher III J. S., 2008, *ApJ*, **674**, 258
- Faucher-Giguère C.-A., Quataert E., 2012, *MNRAS*, **425**, 605
- Fiore F., et al., 2017, *A&A*, **601**, A143
- Flury S. R., et al., 2022, *ApJ*, **930**, 126
- Flury S. R., Moran E. C., Eleazer M., 2023, *MNRAS*, **525**, 4231
- Flury S. R., Arellano-Córdova K. Z., Moran E. C., Einsig A., 2025a, *MNRAS*, **543**, 3367
- Flury S. R., et al., 2025b, *ApJ*, **985**, 128
- Foreman-Mackey D., 2016, *The Journal of Open Source Software*, **1**, 24
- Foreman-Mackey D., Hogg D. W., Lang D., Goodman J., 2013, *PASP*, **125**, 306
- Fukui Y., Sugitani K., Takaba H., Iwata T., Mizuno A., Ogawa H., Kawabata K., 1986, *ApJ*, **311**, L85
- García-Benito R., Pérez E., Díaz Á. I., Maíz Apellániz J., Cerviño M., 2011, *AJ*, **141**, 126
- Geen S., Pellegrini E., Bieri R., Klessen R., 2020, *MNRAS*, **492**, 915
- Geen S., Bieri R., de Koter A., Kimm T., Rosdahl J., 2023, *MNRAS*, **526**, 1832
- Harper-Clark E., Murray N., 2009, *ApJ*, **693**, 1696
- Harrison C. M., Alexander D. M., Mullaney J. R., Swinbank A. M., 2014, *MNRAS*, **441**, 3306
- Hawcroft C., et al., 2025, *arXiv e-prints*, p. [arXiv:2505.24841](https://arxiv.org/abs/2505.24841)
- Heckman T. M., Miley G. K., van Breugel W. J. M., Butcher H. R., 1981, *ApJ*, **247**, 403
- Heckman T. M., Armus L., Miley G. K., 1990, *ApJS*, **74**, 833
- Heckman T. M., Dahlem M., Lehnert M. D., Fabbiano G., Gilmore D., Waller W. H., 1995, *ApJ*, **448**, 98
- Heckman T. M., Alexandroff R. M., Borthakur S., Overzier R., Leitherer C., 2015, *ApJ*, **809**, 147
- Hirano N., Kameya O., Kasuga T., Umemoto T., 1992, *ApJ*, **390**, L85
- Hjelm M., Lindblad P. O., 1996, *A&A*, **305**, 727
- Hjerting F., 1938, *ApJ*, **88**, 508
- Hogarth L., et al., 2020, *MNRAS*, **494**, 3541
- Hunter J. D., 2007, *Computing in Science Engineering*, **9**, 90
- Icke V., 1981, *ApJ*, **247**, 152
- Ilee J. D., Cyganowski C. J., Nazari P., Hunter T. R., Brogan C. L., Forgan D. H., Zhang Q., 2016, *MNRAS*, **462**, 4386
- Ipavich F. M., 1975, *ApJ*, **196**, 107
- Ishibashi W., Fabian A. C., Maiolino R., 2018, *MNRAS*, **476**, 512
- Izotov Y. I., Thuan T. X., Lipovetsky V. A., 1997, *ApJS*, **108**, 1
- James B. L., et al., 2022, *ApJS*, **262**, 37
- Jaskot A. E., Oey M. S., Scarlata C., Dowd T., 2017, *ApJ*, **851**, L9
- Jaskot A. E., Dowd T., Oey M. S., Scarlata C., McKinney J., 2019, *ApJ*, **885**, 96
- Jennings R. M., et al., 2025, *ApJ*, **979**, 64
- Kaufman V., Martin W. C., 1993, *Journal of Physical and Chemical Reference Data*, **22**, 279
- Kelleher D. E., Podobedova L. I., 2008, *Journal of Physical and Chemical Reference Data*, **37**, 1285
- Kobayashi C., Karakas A. I., Lugaro M., 2020, *ApJ*, **900**, 179
- Komarova L., Oey M. S., Krumholz M. R., Silich S., Kumari N., James B. L., 2021, *ApJ*, **920**, L46
- Komarova L., et al., 2025, *arXiv e-prints*, p. [arXiv:2506.19623](https://arxiv.org/abs/2506.19623)
- Kramida A., Yu. Ralchenko Reader J., and NIST ASD Team 2024, NIST Atomic Spectra Database (ver. 5.12), [Online]. Available: <https://physics.nist.gov/asd> [2025, June 3]. National Institute of Standards and Technology, Gaithersburg, MD.
- Krogager J.-K., 2018, *arXiv e-prints*, p. [arXiv:1803.01187](https://arxiv.org/abs/1803.01187)
- Krumholz M. R., Thompson T. A., Ostriker E. C., Martin C. L., 2017, *MNRAS*, **471**, 4061
- Lamers H. J. G. L. M., Morton D. C., 1976, *ApJS*, **32**, 715
- Lamers H. J. G. L. M., Cerruti-Sola M., Perinotto M., 1987, *ApJ*, **314**, 726
- Lancaster L., Kim J.-G., Bryan G. L., Menon S. H., Ostriker E. C., Kim C.-G., 2025a, *arXiv e-prints*, p. [arXiv:2505.22730](https://arxiv.org/abs/2505.22730)
- Lancaster L., Kim C.-G., Kim J.-G., Ostriker E. C., Bryan G. L., 2025b, *arXiv e-prints*, p. [arXiv:2505.22733](https://arxiv.org/abs/2505.22733)
- Laurie D. P., 1997, *Mathematics Of Computation*, **66**, 24
- Leitherer C., et al., 1999, *ApJS*, **123**, 3
- Leitherer C., Ekström S., Meynet G., Schaerer D., Agienko K. B., Levesque E. M., 2014, *ApJS*, **212**, 14
- Leroy A. K., et al., 2015, *ApJ*, **814**, 83
- Lieb E. P., et al., 2025, *ApJ*, **979**, L3
- Liu G., Zakamska N. L., Greene J. E., Nesvadba N. P. H., Liu X., 2013, *MNRAS*, **436**, 2576
- Liu W., Veilleux S., Canalizo G., Rupke D. S. N., Manzano-King C. M., Bohn T., U V., 2020, *ApJ*, **905**, 166
- López-Sánchez Á. R., Esteban C., García-Rojas J., Peimbert M., Rodríguez M., 2007, *ApJ*, **656**, 168
- Lopez L. A., Krumholz M. R., Bolatto A. D., Prochaska J. X., Ramirez-Ruiz E., 2011, *ApJ*, **731**, 91
- Louvet F., Dougados C., Cabrit S., Mardones D., Ménard F., Tabone B., Pinte C., Dent W. R. F., 2018, *A&A*, **618**, A120
- Lucy L. B., 1971, *ApJ*, **163**, 95
- Lucy L. B., Solomon P. M., 1970, *ApJ*, **159**, 879
- Luminari A., Piconcelli E., Tombesi F., Zappacosta L., Fiore F., Piro L., Vagnetti F., 2018, *A&A*, **619**, A149
- Luminari A., Piconcelli E., Tombesi F., Nicastro F., Fiore F., 2024, *A&A*, **691**, A357
- Luridiana V., Morisset C., Shaw R. A., 2015, *A&A*, **573**, A42
- Lynden-Bell D., Rees M. J., 1971, *MNRAS*, **152**, 461
- Mainali R., et al., 2022, *ApJ*, **940**, 160
- Maiolino R., et al., 2012, *MNRAS*, **425**, L66
- Manara C. F., Ansdell M., Rosotti G. P., Hughes A. M., Armitage P. J., Lodato G., Williams J. P., 2023, in Inutsuka S., Aikawa Y., Muto T., Tomida K., Tamura M., eds, *Astronomical Society of the Pacific Conference Series Vol. 534, Protostars and Planets VII*. p. 539 ([arXiv:2203.09930](https://arxiv.org/abs/2203.09930)), doi:[10.48550/arXiv.2203.09930](https://doi.org/10.48550/arXiv.2203.09930)
- Marlowe A. T., Heckman T. M., Wyse R. F. G., Schommer R., 1995, *ApJ*, **438**, 563
- Martin C. L., 1998, *ApJ*, **506**, 222
- Martin C. L., Shapley A. E., Coil A. L., Kornei K. A., Murray N., Pancoast A., 2013, *ApJ*, **770**, 41
- Martin C. L., Peng Z., Li Y., 2024, *ApJ*, **966**, 190
- Mathews W. G., 1974, *ApJ*, **189**, 23
- Matzeu G. A., et al., 2022, *MNRAS*, **515**, 6172
- McQuinn K. B. W., van Zee L., Skillman E. D., 2019, *ApJ*, **886**, 74
- Mehdipour M., et al., 2017, *A&A*, **607**, A28
- Mehdipour M., et al., 2025, *A&A*, **699**, A228
- Menon S. H., Burkhardt B., Somerville R. S., Thompson T. A., Sternberg A., 2024, *arXiv e-prints*, p. [arXiv:2408.14591](https://arxiv.org/abs/2408.14591)
- Mihalas D., Kunasz P. B., Hummer D. G., 1975, *ApJ*, **202**, 465
- Morton D. C., 2003, *ApJS*, **149**, 205
- Müller-Sánchez F., Prieto M. A., Hicks E. K. S., Vives-Arias H., Davies R. I., Malkan M., Tacconi L. J., Genzel R., 2011, *ApJ*, **739**, 69
- Murray N., Quataert E., Thompson T. A., 2005, *ApJ*, **618**, 569
- Netzer H., 1982, *MNRAS*, **198**, 589
- Noerdlinger P. D., Rybicki G. B., 1974, *ApJ*, **193**, 651
- Norris J. P., Bonnell J. T., Kazanas D., Scargle J. D., Hakkila J., Giblin T. W., 2005, *The Astrophysical Journal*, **627**, 324
- Oey M. S., Clarke C. J., 1997, *MNRAS*, **289**, 570
- Olivier G. M., Berg D. A., Chisholm J., Erb D. K., Pogge R. W., Skillman E. D., 2022, *ApJ*, **938**, 16
- Osterbrock D., Ferland G., 2006, *Astrophysics of Gaseous Nebulae and Active Galactic Nuclei*. University Science Books
- Owoccki S., 2025, *arXiv e-prints*, p. [arXiv:2507.18721](https://arxiv.org/abs/2507.18721)
- P. Virtanen R., Gommers T. O., 2020, *Nature Methods*, **17**, 261–272
- Padgett D. L., Brandner W., Stapelfeldt K. R., Strom S. E., Terebey S., Koerner D., 1999, *AJ*, **117**, 1490
- Parker K. S., et al., 2024, *ApJ*, **977**, 104
- Parker K. S., et al., 2025, *arXiv e-prints*, p. [arXiv:2511.15869](https://arxiv.org/abs/2511.15869)

- Pauldrach A., Puls J., Kudritzki R. P., 1986, *A&A*, **164**, 86
- Peimbert M., Peimbert A., Delgado-Inglada G., 2017, *Publications of the Astronomical Society of the Pacific*, **129**, 082001
- Pelat D., Alloin D., 1980, *A&A*, **81**, 172
- Pelat D., Alloin D., Fosbury R. A. E., 1981, *MNRAS*, **195**, 787
- Peng Z., Martin C. L., Thibodeaux P., Zhang J., Hu W., Li Y., 2023, *ApJ*, **954**, 214
- Peng Z., et al., 2025, *ApJ*, **981**, 171
- Phillips M. M., Turtle A. J., Edmunds M. G., Pagel B. E. J., 1983, *MNRAS*, **203**, 759
- Podobedova L. I., Kelleher D. E., Wiese W. L., 2009, *Journal of Physical and Chemical Reference Data*, **38**, 171
- Poynting J. H., 1904, *Philosophical Transactions of the Royal Society of London Series A*, **202**, 525
- Prochaska J. X., Kasen D., Rubin K., 2011, *ApJ*, **734**, 24
- Puls J., Najarro F., Sundqvist J. O., Sen K., 2020, *A&A*, **642**, A172
- Quataert E., 2004, *ApJ*, **613**, 322
- Quataert E., Jiang Y.-F., Thompson T. A., 2022a, *MNRAS*, **510**, 920
- Quataert E., Thompson T. A., Jiang Y.-F., 2022b, *MNRAS*, **510**, 1184
- Rich J. A., Dopita M. A., Kewley L. J., Rupke D. S. N., 2010, *ApJ*, **721**, 505
- Rivera-Thorsen T. E., et al., 2015, *ApJ*, **805**, 14
- Rupke D. S. N., Veilleux S., 2013, *ApJ*, **768**, 75
- Rupke D. S., Veilleux S., Sanders D. B., 2005a, *ApJS*, **160**, 87
- Rupke D. S., Veilleux S., Sanders D. B., 2005b, *ApJS*, **160**, 115
- Rusakov V., et al., 2025, *arXiv e-prints*, p. arXiv:2503.16595
- Rybicki G. B., Hummer D. G., 1983, *ApJ*, **274**, 380
- Rybicki G. B., Lightman A. P., 1979, *Radiative processes in astrophysics*
- Sander A. A. C., Hamann W. R., Todt H., Hainich R., Shenar T., 2017, *A&A*, **603**, A86
- Scarlata C., Panagia N., 2015, *ApJ*, **801**, 43
- Sher D., 1968, *J. R. Astron. Soc. Canada*, **62**, 105
- Sim S. A., Long K. S., Miller L., Turner T. J., 2008, *MNRAS*, **388**, 611
- Sim S. A., Miller L., Long K. S., Turner T. J., Reeves J. N., 2010, *MNRAS*, **404**, 1369
- Sirianni M., Nota A., Pasquali A., Clampin M., 1998, *A&A*, **335**, 1029
- Skillman E. D., 1985, *ApJ*, **290**, 449
- Sobolev V. V., 1944, *Soviet Ast.*, **21**, 1944
- Sobolev V. V., 1957, *Soviet Ast.*, **1**, 678
- Sobolev V. V., 1960, *Moving envelopes of stars*
- Sramek R. A., Weedman D. W., 1986, *ApJ*, **302**, 640
- Steidel C. C., Erb D. K., Shapley A. E., Pettini M., Reddy N., Bogosavljević M., Rudie G. C., Rakic O., 2010, *ApJ*, **717**, 289
- Stock D. J., Barlow M. J., Wesson R., 2011, *MNRAS*, **418**, 2532
- Storey P. J., Zeippen C. J., 2000, *MNRAS*, **312**, 813
- Suzuki T. K., Inutsuka S.-i., 2009, *ApJ*, **691**, L49
- Tayal S. S., Zatsarinny O., 2010, *ApJS*, **188**, 32
- Telford O. G., Chisholm J., Sander A. A. C., Ramachandran V., McQuinn K. B. W., Berg D. A., 2024, *ApJ*, **974**, 85
- Tenorio-Tagle G., Munoz-Tunon C., Cid-Fernandes R., 1996, *ApJ*, **456**, 264
- Tepper-García T., 2006, *MNRAS*, **369**, 2025
- Thomas A. D., et al., 2017, *ApJS*, **232**, 11
- Thompson T. A., Heckman T. M., 2024, *ARA&A*, **62**, 529
- Thompson T. A., Fabian A. C., Quataert E., Murray N., 2015, *MNRAS*, **449**, 147
- Tumlinson J., Peebles M. S., Werk J. K., 2017, *ARA&A*, **55**, 389
- Vander Meulen B., Camps P., Tsujimoto M., Wada K., 2024, *A&A*, **688**, L33
- Veilleux S., 1991, *ApJS*, **75**, 383
- Veilleux S., Shopbell P. L., Miller S. T., 2001, *AJ*, **121**, 198
- Veilleux S., Maiolino R., Bolatto A. D., Aalto S., 2020, *A&ARv*, **28**, 2
- Venturi G., et al., 2018, *A&A*, **619**, A74
- Vink J. S., Sander A. A. C., 2021, *MNRAS*, **504**, 2051
- Vink J. S., de Koter A., Lamers H. J. G. L. M., 2001, *A&A*, **369**, 574
- Weaver R., McCray R., Castor J., Shapiro P., Moore R., 1977, *ApJ*, **218**, 377
- Wehrle A. E., Morris M., 1988, *AJ*, **95**, 1689
- Whittle M., 1985, *MNRAS*, **213**, 1
- Xrism Collaboration et al., 2025, *Nature*, **641**, 1132
- Yarovova A. D., Gerasimov I. S., Egorov O. V., Moiseev A. V., Vasiliev K. I., Lozinskaya T. A., 2025, *arXiv e-prints*, p. arXiv:2507.08651
- Yoshida M., Kawabata K. S., Ohyama Y., 2011, *PASJ*, **63**, S493
- Zheng W., Binette L., Sulentic J. W., 1990, *ApJ*, **365**, 115
- de Valon A., Dougados C., Cabrit S., Louvet F., Zapata L. A., Mardones D., 2020, *A&A*, **634**, L12
- van der Walt S., Colbert S. C., Varoquaux G., 2011, *Computing in Science Engineering*, **13**, 22

APPENDIX A: GEOMETRY OF DIRECTED OUTFLOWS

To determine the integral $2\pi\ell_w$ over the azimuthal coordinate term in $d\Omega$, for a directed conical outflow, we must first project the spherical cap of a cone onto the plane of the sky. Then, we must subsequently compute the fraction ℓ_w of a given deprojected velocity (w) subtended by the cap. With this formalism in hand, we demonstrate incorporation of additional geometric components in the form of cavities and obstructing disks.

A1 Cones As A Spherical Cap Projection

An outflowing cone on the plane of the sky appears as a the projected spherical cap with axes g and h and is offset from the projected outflow source by some distance S . These quantities can be expressed in terms of the inclination and opening angle of the outflow center such that

$$S = \sin i \cos \theta \quad (\text{A1})$$

$$g = \sin \theta \quad (\text{A2})$$

$$h = \cos i \sin \theta. \quad (\text{A3})$$

We illustrate a single case of such a projection in Figure A1. In the case where $i + \theta > 90^\circ$, the projection is no longer an ellipse but rather an ellipse plus a lune to account for the projection of the ‘‘top’’ of the spherical cap and an additional lune to the opposing side to account for the projection of the second cone. We visualize such a scenario in the last two panels of Figure A2.

A2 Cone Inscription of Deprojected Velocities

The fractional arc length ℓ_w of the deprojected velocity inscribed by the cone can be determined by solving the system of linear equations for a circle and the projected spherical cap area to determine where they intersect, which in turn determine the bounds on the integral(s) over the azimuthal coordinate of the solid angle. The azimuthal ‘‘ring’’ of gas with velocity w has a radius r_w defined by the sine of the angle ρ between the observed and deprojected velocities u and w , respectively. Relativistic aberration (i.e., beaming effect) is invariant across the azimuthal angle, ergo a classical treatment in the source frame is still accurate for deriving the geometry of the projected cone. The apparent deprojection radius r_w for each azimuthal ring is thus

$$r_w = \sqrt{1 - \left(\frac{u}{w}\right)^2}, \quad (\text{A4})$$

which we show in Figure A1. Solving the system of equations of the projected cap and the deprojected velocity ring gives intersection points of (p, q) such that

$$p = \pm \sqrt{r_w^2 - q^2} \quad (\text{A5})$$

and, from substituting p and employing the quadratic equation,

$$q = \frac{-B \pm \sqrt{B^2 - 4AC}}{2A} \quad (\text{A6})$$

where the coefficients are

$$A = \left(\frac{g}{h}\right)^2 - 1 \quad (\text{A7})$$

$$B = -2S \left(\frac{g}{h}\right)^2 \quad (\text{A8})$$

$$C = r_w^2 + \left(\frac{gS}{h}\right)^2 - g^2. \quad (\text{A9})$$

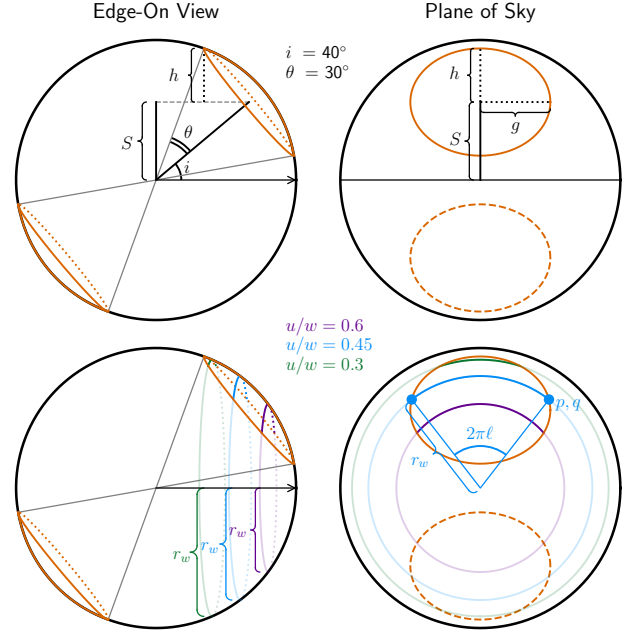


Figure A1. A cone geometry in the case of $i = 40^\circ$, $\theta = 30^\circ$. Left panels illustrate the cones seen edge-on, i.e., transverse to the line of sight. Right panels illustrate the cones seen face-on, i.e., projected onto the plane of the sky. Solid ellipses indicates the cone projected anterior to source relative to the observe while dashed ellipses indicate the posterior projection. Top panels illustrate the geometric terms S , g , and h which translate the opening angle θ and inclination i of the cones into a projection onto the sky. Bottom panels illustrate how an observed velocity u de-projects into an azimuthal band with radius r_w with unique azimuthal coverage $\pi\ell$ within the cone defined by the intersection points p, q of the velocity band with the projected cone. High u/w (low r_w) corresponds to wings of a line profile far from the systemic velocity while low u/w (high r_w) corresponds to the core of the line profile close to the systemic velocity.

To reduce computation time, A and B are calculated outside of the integral as only C depends on the de-projected velocity w . The intersection points (p, q) given by A , B , and C yield the arc of the enclosed deprojected velocity such that

$$\pi\ell_w = \begin{cases} \arccos \frac{q}{r_w} & q > 0 \\ \pi - \arccos \frac{q}{r_w} & q < 0 \end{cases} \quad (\text{A10})$$

which notably avoids the additional step of calculating p . We illustrate such a solution for $\pi\ell$, including the velocity dependence, in Figure A1. If multiple real solutions for (p, q) exist due to the lune from the projection of the second cone into the plane, then OutLines simply sums the two arcs.

We show example projections in Figure A2 for several values of u/w , i , and θ . As a tool, we also include in OutLines a module to produce such visualizations for any given combination of i and θ . Calling `OutLines.PlotConeProjection(i, theta0)` will draw the geometry and projection as shown in Figure A2 for any inclination and opening angle.

A3 Cavity Effects

As discussed in §2.4, some outflows exhibit a bidirectional cones with cavities, resulting in a hollow cone geometry. The fractional arc length ℓ_{cavity} lost due to the cavity can be calculated in the same

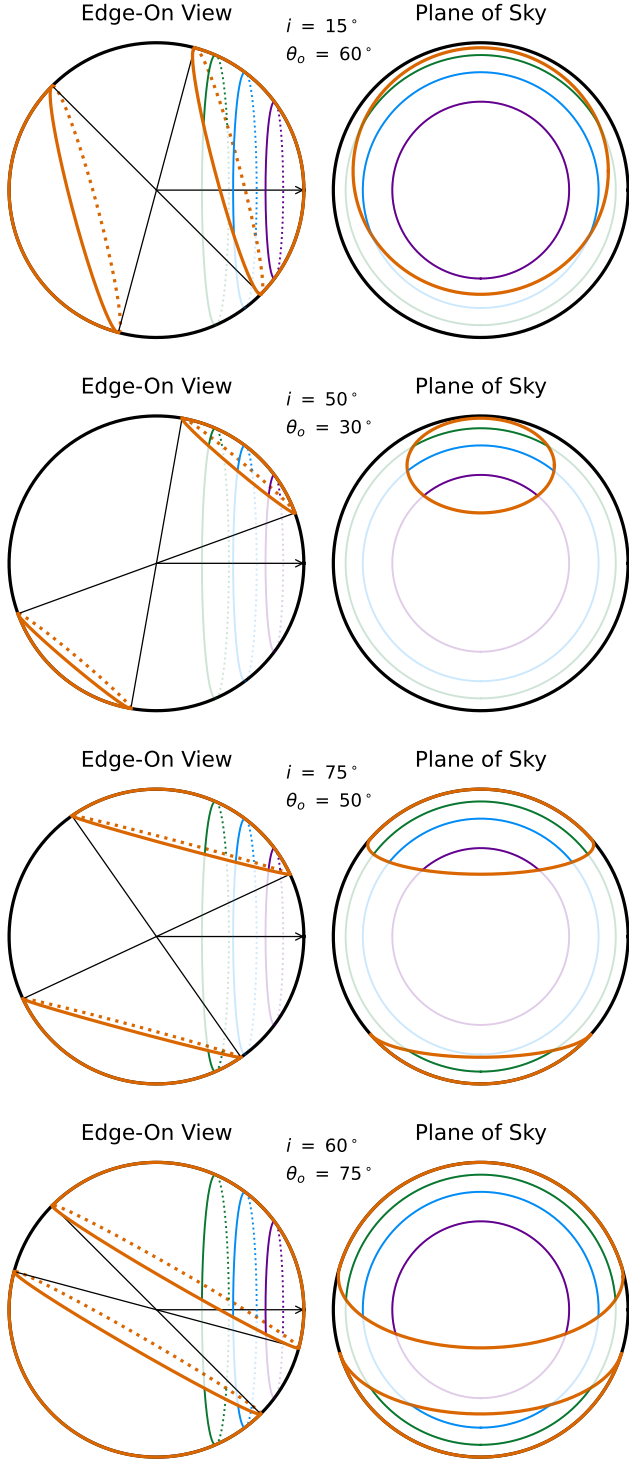


Figure A2. Following Figure 14, we illustrate bidirectional cone geometries (left of each panel) projected onto the plane of the sky (right of each panel) for various combinations of i and θ_o (orange). Circles indicate deprojected velocities of $u/w = 0.4$ (green), 0.6 (blue), and 0.8 (purple). Opaque segments indicate where a deprojected velocity is inscribed by the projected spherical cap. Arrow in the left of each panel indicates direction of the projections onto the plane of the sky (i.e., the line of sight).

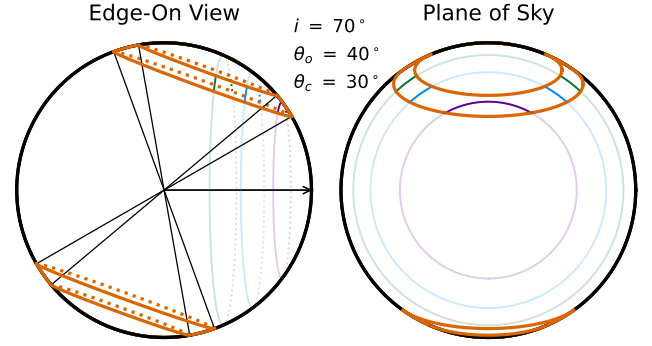


Figure A3. Same as Figure A2 but for directed cones with an inner cavity.

manner as ℓ_w and subtracted, which we show in Figure A3. Calling `OutLines.PlotConeProjection(i, theta0, thetaC)` will illustrate projections similar to those of the filled cones but for the hollow cone geometry.

A4 Obstruction by a Disk

In §2.4, we present the possible inclusion of a disk which encircles the source of the outflow and is inclined orthogonally to a cone or hemisphere axis. This disk obstructs the posterior cone or hemisphere but may affect either the red-shifted or both wings of the line profile. `OutLines` projects the disk onto the line of sight and then determines the length of each deprojected velocity which is still observed after accounting for the disk effect. Since the disk is centered at the source of the outflow and assumed to be orthogonal to the outflow cone, the projected disk is simply an ellipse with semi-major and semi-minor axes of $(w[x_d|\beta], w[x_d|\beta] \cos i)$. Thus, the intersection points (p_d, q_d) between the deprojected velocity and the disk can be written as

$$p_d = \pm \sqrt{r_w^2 - q_d^2} \quad (\text{A11})$$

and

$$q_d = \pm \sqrt{\frac{r_w^2 - w^2[x_d|\beta]}{\sec^2 i - 1}}. \quad (\text{A12})$$

Rather than compute ℓ_w and ℓ_{disk} separately, which would needlessly incur a computational overhead, we can instead simply compare q and q_d to determine the final ℓ_w . For the posterior cone or hemisphere, ℓ_w is given by

$$\pi \ell_w = \begin{cases} \arccos \frac{q}{r_w} & q > q_d \\ \arccos \frac{q_d}{r_w} & -q_d < q < q_d \\ 2 \arccos \frac{q_d}{r_w} - \arccos \frac{q}{r_w} & q < -q_d \end{cases}. \quad (\text{A13})$$

If q has multiple solutions due to the projected lune from the anterior cone, `OutLines` will add to ℓ_w the first case evaluated using the second solution for q with the imposition that $q > q_d$ since the anterior cone is not obstructed by the disk. Note that, in the case of $i + \theta > 90^\circ$, the red component will never be fully obstructed. For the anterior cone, ℓ_w is given by

$$\pi \ell_w = \begin{cases} \arccos \frac{q}{r_w} & q > 0, q_1 > q_d \\ \arccos \frac{q_d}{r_w} & q > 0, q_1 < q_d \\ \pi - \arccos \frac{q}{r_w} & q < 0 \end{cases}. \quad (\text{A14})$$

where the q_1 criterion only applies in the case of a lune projected from the posterior cone, which can be obstructed by the disk. Note that, in the case of $i + \theta > 90^\circ$, the blue component can be partially obstructed, primarily affecting the line core. Under this formalism, ℓ_{cavity} can still be subtracted to determine the hollow cone geometry as both ℓ_w and ℓ_{cavity} will account for any disk effects on the deprojected velocity apriori.

APPENDIX B: IMPLEMENTATION OF OUTLINES

B1 Installation

Installing OutLines can be done in the terminal command line using `pip` as shown below.

```
! pip3 install SpecOutLines
```

Alternatively, the GitHub repository can be cloned as below

```
! git clone https://github.com/sflury/OutLines.git
```

Dependencies include `python >=3.12.9`, which may require updating of python globally or creating, say, an `anaconda` environment. Other dependencies, including `numpy`, `scipy`, and `matplotlib` will be automatically managed by `pip`, including within `conda` environments.

B2 The Profile Classes

The primary front-end user interaction with OutLines is through the various `Profile` object classes, which we list in Table B1. Calling one of these classes instantiates an object containing the line profile model, parameter guesses, and parameter bounds. When calling a class, users need only provide the relevant atomic data and any optional keyword arguments specifying the velocity field, geometry, and density profile to customize the model (see Table B1). The terms and related keyword arguments for the profile model are listed in Table B2 for the geometry, Table B3 for the velocity field, and Table B4 for the density profile, with the OutLines defaults indicated by a †. In some cases, users may want to consider a velocity field or density profile not included in OutLines. In such cases, if a user passes a function to either keyword instead of a string, OutLines will implement the user-defined field or profile.

Users will primarily use OutLines by instantiating one of the several `Profile` classes: `Nebular`, `Resonant`, `Fluorescent`, and `Absorption`. The object-bound methods of the `Profile` classes can be used to obtain or update parameter values and to generate line profiles. We provide examples of using these classes to generate line profiles in Appendix C. To obtain line profiles computed by OutLines, users can call the `get_profile()` bound method for either class, which requires only an array of wavelengths and computes a line profile for the parameters stored in the object. Alternatively, the line profile function is directly accessible through the `Profile` attribute, which requires a wavelength array just as `get_profile()` but also takes the full set of parameters. For purposes of modeling observations, users may prefer to use the `Profile` function where the input parameters may be readily varied without updating the corresponding attribute in the object.

The `get_params()` and `get_bounds()` methods will pass the relevant values from the object to the user. The `print_settings()`, `print_params()`, and `print_bounds()` will print the selected profile settings (velocity field, geometry, density profile, and optional static line component), the corresponding current parameters, and the associated boundaries. The `update_params()` and

`update_bounds()` methods will allow users to update any of the profile parameters and their related bounds. All `Profile` classes can each support multiple lines, something we encourage users to consider.

B3 The Properties Class

After modeling a wind or outflow from observed spectral lines, users will want to derive important diagnostic properties to determine what drives the wind, how, and to what extent the outflow impacts its environment. Because the relevant information is already contained in the `Profile` classes, `Properties` is designed to inherit one of the `Profile` classes and will automatically compute relevant properties defined in 2.5, with the caveat that n_0 and R_0 remain unknown.

Users can access these results directly from the object class once instantiated, either through the stored dictionary or by printing to the command line via the bound method `print_propts()`. As with the `Emission` and `Absorption` classes, `Properties` also has the bound method `update_params()`, which behaves similar to the bound method in the `Profile` classes by allowing users to change parameters associated with the line profile.

B4 Visualization

To assist with interpretation of outflow properties and geometry, OutLines contains several functions to generate figures like the ones presented here. To produce isocontours as in Figure 6, we provide the `PlotIsoContours` function. To produce the edge-on geometric cartoon as in Figure 10, we provide the `PlotGeometry` function. To produce the cone and velocity projection geometry for filled cones as in Figure A1, we provide the `PlotProjGeom` function. To produce the velocity projections for filled and hollow cones as in Figures A2 and A3, we provide the `PlotConeProj` function.

B5 Numerical Methods

Some equations require root-finding where analytic solutions are not possible, including the “source-effect” and aperture velocity limits (Equations 32 and 34, respectively) and the characteristic outflow radius x_{out} where the momentum density is maximized. As in Flury et al. (2023), we employ Brent’s method implemented by `scipy.optimize` to solve for the root in each case.

The initial profile model of Flury et al. (2023) solved the integral for the emission line profile (Equation 10) using the adaptive Romberg method, which included Richardson extrapolation under the Bulirsch-Stoer method. As implemented by the now-deprecated `scipy.integrate.romberg`, this method can be costly and in later `scipy` versions has loss of accuracy in non-spherical geometries due to poor sampling of the integrand. For improvements to both speed and accuracy, we now adopt Gauss-Legendre quadrature with a fixed number of nodes to solve the integrals for ϕ_λ . We implement quadrature integration following the `scipy.integrate.fixed_quad`; however, for speed, we have pre-computed the nodes and weights using `scipy.special.roots_legendre`, which takes ≈ 1 ms for each call to `scipy.integrate.fixed_quad`. We find at least 16 nodes necessary to obtain reliable profile solutions in many cases but conservatively assume 96 nodes for optimal accuracy across the profile parameter spaces without significant computational expense. For bubbles, we restrict velocity bounds where possible to improve sampling of the density profile. Future work may include adopting

Table B1. *Left:* the Profile object classes in OutLines with which users can generate model profiles for different spectral line types. *Right:* keyword settings for the Profile classes to customize models. Disk not implemented for spherical geometries. Pulse only applicable ensemble density profiles.

class	use	atomic data	keywords	options	default
Nebular	nebular emission lines	λ_0	Geometry	Table B2	Spherical
Resonant	resonant emission lines	λ_0, f, p_r	VelocityField	Table B3	BetaCAK
Fluorescent	fluorescent emission lines	λ_0, f, p_r, p_f	DensityProfile	Table B4	PowerLaw
Absorption	resonant absorption lines	λ_0, f	AddStatic	boolean	False
			FromRest	boolean	True
			Disk	boolean	False
			Aperture	boolean	False
			Pulse	Table B4	'Normal'
				Bubbles/Shells	

Table B2. Geometry keyword options and related required arguments for OutLines. † indicates the OutLines default.

Geometry	terms	assumptions
'Spherical' †	none	$i = 0, \theta_c = 0^\circ, \theta_o = 90^\circ$
'Hemisphere'	i	$\theta_c = 0^\circ, \theta_o = 90^\circ$
'FilledCones'	i, θ_o	$\theta_c = 0^\circ$
'HollowConesFixedCavity'	i, θ_o	$\theta_c = \theta_o - 10^\circ$
'HollowCones'		
'OpenCones'	i, θ_c, θ_o	none

Table B3. Velocity field keyword options for OutLines, each parameterized by an exponent β . † indicates the OutLines default.

VelocityField	equation	references
'BetaCAK' †	15	Castor et al. (1975a); Castor & Lamers (1979)
'AccPlaw'	16	Steidel et al. (2010)
'VelPlaw'	17	Faucher-Giguère & Quataert (2012)

Table B4. Density profile keyword options and related required arguments for OutLines. † indicates the OutLines default.

DensityProfile	terms	equation
Winds		
'PowerLaw' †	α	19
'Exponential'	γ	20
'DoublePowerLaw'	α_1, α_2, x_1	21
Bubbles / Shells		
'Normal'	x_1, σ_x	22
'LogNormal'	$\log x_1, \log \sigma_x$	23
'DLogic'	$\log x_1, k$	25
'Shell'	x_1, σ_x	26
'FRED'	x_1, τ_1, τ_2	24
Ensembles		
'Pulses'	x_1, σ_x, x_k	27
'DampedPulses'	$\gamma, x_1, \sigma_x, x_k$	28

Table B5. Outflow properties computed by the OutLines.Properties object class. Property names listed here correspond to the dictionary keys in props attribute and the terminal output by print_props method.

name	equation	property
x.out		x_{out} characteristic radius
v.out	36	v_{out} characteristic radius
Rcal	37	\mathcal{R} relative column density
Mdot	41	$\dot{M}/n_0 R_0^2$ mass outflow rate
pdot	42	$\dot{p}/n_0 R_0^2$ momentum flux
Edot	43	$\dot{E}/n_0 R_0^2$ mechanical luminosity

Gauss-Kronrod integration for improved accuracy and precision, e.g., following Laurie (1997).

To normalize the line profile, we use a linear integration method to effectively handle cusps which may occur at peaks and troughs, typically near the line core. We implement this integration following the shoelace algorithm case of Green's theorem. Benchmarking against the scipy.integrate.trapezoid implementation of trapezoid rule integration, we find comparable results with a marginally faster (by < 1 ms) compute time.

For a single core on a conventional laptop computer, benchmarking indicates that OutLines can calculate an emission line profile at $R = 5,000$ in 6 ms for the most complex geometry (disk plus hollow cones), and that the compute time increases almost linearly with R such that run times are 2.5 ms at $R = 2,000$, 4 ms at $R = 3,000$, 13 ms at $R = 10,000$, 25 ms at $R = 20,000$, and 65 ms at $R = 50,000$. For the simplest geometry (spherical), the compute times are much faster (< 1 ms for $R \leq 30,000$). Given reasonable guess parameters, iterative non-linear least squares fitting routines like the trust-reflective algorithm (see scipy.optimize.least_squares) perform rapidly, typically converging on a solution within 10 to 30 s depending on the data and the assumed model. For 25 walkers, a typical MCMC sampler (here benchmarked using emcee, Foreman-Mackey et al. 2013) takes anywhere from 0.1 to 2 s per step to run on a conventional laptop computer when fitting an OutLines model to an observed line profile, even when accounting for complex geometries and LSF effects. The addition of convolution with a line spread function does increase the computation time; however, the extent to which this occurs depends on the resolution, size of the data set, and the implementation of the convolution.

APPENDIX C: EXAMPLE LINE PROFILES WITH OUTLINES

Below, we provide example usages of the Absorption, Nebular, and Fluorescent line profile object classes in OutLines. We demonstrate how to select different options for the line profile model, update model parameters and bounds associated with the line profile, display documentation, print various model settings and parameters, and extract computed line profiles for visualization. We also demonstrate how to compute outflow properties from the Properties class and print the results to the command line.

C1 C II $\lambda 1334$

Example instantiations of Absorption, Resonant, and Fluorescent objects from the Profile class using atomic data from Morton (2003). Here, the object classes are instantiated, documentation, setting, and parameters are printed to the terminal, and the column density and terminal velocity are updated.

```

1 # import the OutLines package
2 import OutLines as OL
3 # instantiate the absorption line
4 # Profile object class
5 modelAbs = OL.Absorption(1334.519,0.128)
6 # print documentation of the model object
7 modelAbs.docs()
8 # print model settings
9 modelAbs.print_settings()
10 # print the current parameters
11 model.print_params()
12 # instantiate the resonant and fluorescent
13 # Profile object classes
14 modelRes = OL.Resonant(1334.532,0.128,0.456)
15 modelFlu = OL.Fluorescent(1335.663,0.115,0.456,0.544)
16 # updates for all three objects
17 for model in [modelAbs,modelRes,modelFlu]:
18     # change the log column density to 1e15 cm^-2
19     model.update_params('LogColumnOutflow1',15)
20     # change the velocity to 500 km s^-1
21     model.update_params('TerminalVelocity', 500.00)
    
```

C2 [O III] $\lambda\lambda 4959, 5007$

Example instantiation of the Nebular object from the Profile class in OutLines using atomic data from NIST (Kramida et al. 2024) and Storey & Zeppen (2000). Here, we illustrate how to customize the model with keyword arguments passed to the object class on instantiation, updating parameters, printing setting and parameters, computing and printing outflow properties, and visualizing a line profile as in Figure C1.

```

1 # import packages
2 import OutLines as OL
3 from numpy import linspace
4 import matplotlib.pyplot as plt
5 # instantiate the nebular line
6 # profile object
7 kwargs = dict(Geometry='HollowCones',AddStatic=True,\
    VelocityField='AccPlaw',Disk=True)
8 model = OL.Nebular([4958.911,5006.843],**kwargs)
9 # update some parameters
10 model.update_params(['TerminalVelocity'],[500,30,15,45])
11 model.update_params(['OpeningAngle','CavityAngle',\
    'Inclination'],[30,15,45])
12 model.update_params(['FluxOutflow1','FluxStatic1'],\
    [1/2.98,1/2.98]) # Storey & Zeppen 2000
13 # print model settings and current parameters
14 model.print_settings()
15 model.print_params()
16 # compute outflow properties
17 props = OL.Properties(model)
18 # print outflow properties
19 props.print_props()
20 # plot the profile
21 wave = linspace(4950,5015,651)
22 plt.plot(wave,model.get_outflow(wave),label='outflow')
23 plt.plot(wave,model.get_static(wave),label='static')
24 plt.plot(wave,model.get_profile(wave)+0.1,label='total')
25 plt.show()
    
```

APPENDIX D: EXAMPLE MODELING

Below, we provide examples for modeling absorption and nebular emission line features using line profiles computed by OutLines. We

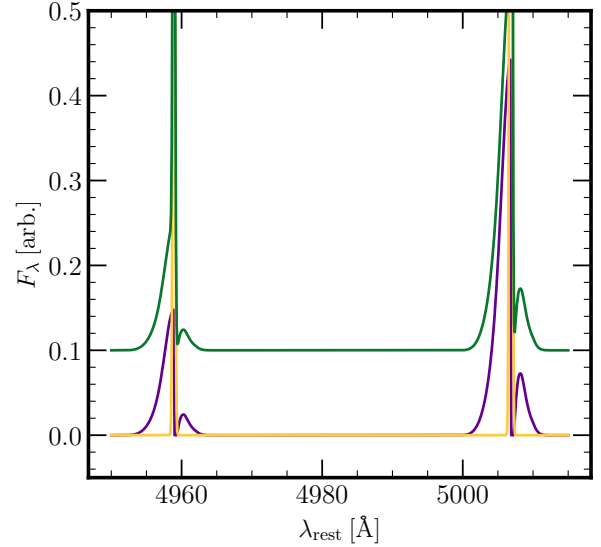


Figure C1. Example [O III] $\lambda\lambda 4959, 5007$ line doublet profile produced using OutLines as shown in Appendix C2.

indicate suggested methods for obtaining best-guess parameters and demonstrate how to use OutLines in tandem with MCMC samplers using the initial value generator and logarithmic posterior probability contained in the object instance of the profile class.

D1 Si II $\lambda\lambda 1190, 1193$ Absorption Doublet

```

1 # import the OutLines package
2 import OutLines as OL
3 # MC sampler for posterior
4 import emcee
5 # wavelength, continuum-subtracted flux, and uncertainty
6 wave,flux,flux_error = data
7 # set up OutLines model using NIST vacuum data
8 kwargs = dict(DensityProfile='DampedPulses',\
    AddStatic=True)
9 model = OL.Absorption([1190.416,1193.290],[0.277,0.575],\
    **kwargs)
10 # initialize walkers and sampler and run the sampler
11 init,nwalk = model.init_params()
12 # run the MCMC sampler
13 sampler = emcee.EnsembleSampler(nwalk,model.npar,\
    model.log_probability,args=(wave,flux,flux_error))
14 sampler.run_mcmc(init,1200,progress=True)
15 samples = sampler.get_chain(discard=200,flat=True)
16 # extract parameters from posterior sample
17 for i,param in enumerate(model.get_param_names()):
18     value = nanquantile(samples[:,i],0.5)
19     model.update_params(param,value)
20 # print line profile parameters to terminal
21 model.print_params()
    
```

D2 [S II] $\lambda\lambda 6716, 6731$ Emission Doublet

```

1 # import the OutLines package
2 import OutLines as OL
3 # scipy nonlinear least squares for initial guess
    
```

```

4 from scipy.optimize import curve_fit
5 # MC sampler for posterior
6 import emcee
7 # wavelength, continuum-subtracted flux, and uncertainty
8 wave, flux, flux_error = data
9 # set up OutLines model using NIST air wavelengths
10 mod_kwargs = dict(AddStatic=True)
11 model = OL.Nebular([6716.440, 6730.815], **mod_kwargs)
12 # simple trust-reflective fit for initial guess
13 tr_kwargs = dict(p0=model.get_params(), \
14                 bounds=model.get_bounds(), sigma=flux_error)
15 p0, c0 = curve_fit(model.Profile, wave, flux, **tr_kwargs)
16 model.update_params(model.get_param_names(), p0)
17 # initialize walkers and sampler and run the sampler
18 init, nwalk = model.init_params()
19 # run the MCMC sampler
20 sampler = emcee.EnsembleSampler(nwalk, model.npar, \
21                               model.log_probability, args=(wave, flux, flux_error))
22 sampler.run_mcmc(init, 1200, progress=True)
23 samples = sampler.get_chain(discard=200, flat=True)
24 # extract parameters from posterior sample
25 for i, param in enumerate(model.get_param_names()):
26     value = nanquantile(samples[:, i], 0.5)
27     model.update_params(param, value)
28 # print line profile parameters to terminal
29 model.print_params()
30 # obtain outflow properties
31 props = OL.Properties(model)
32 # print outflow properties to terminal
33 props.print_props()

```

D3 [O III] λ 4959, 5007 Emission Doublet for the Seyfert 2 in NGC 2992

```

1 # import the OutLines package
2 import OutLines as OL
3 # MethodType for changing prior
4 from types import MethodType
5 # scipy nonlinear least squares for initial guess
6 from scipy.optimize import curve_fit
7 # scipy convolution function for speed
8 from scipy.signal import convolve
9 # MC sampler for posterior
10 import emcee
11 # log prior -- uniform bounded
12 def log_prior(self, theta):
13     tlower, tupper = self.get_bounds()
14     tbound =
15         list(map(self.__fun_bound__, theta, tlower, tupper))
16     # enforce theta_o - theta_c >= 5 degrees
17     # suggest atomic data to within 5%
18     if all(tbound) and theta[8]-theta[9] > 0.087:
19         return -0.5*((theta[4]/theta[3]-2.98)/0.05)**2 \
20             -0.5*((theta[6]/theta[5]-2.98)/0.05)**2
21     else:
22         return -inf
23 # log likelihood for chi squared
24 # including convolution of line profile with LSF
25 # assuming the LSF kernel `kern` is defined
26 def log_likelihood(self, theta, x, y, yerr):
27     ybar =
28         convolve(model.Profile(x, *theta)+cont[ind], kern, 'same')
29     ln_prb = -((y-ybar)/yerr)**2 - 2*log(yerr)
30     return nansum(ln_prb)
31 # instantiate the nebular line
32 # profile object using

```

```

31 # rest wavelengths from NIST
32 kwargs = dict(Geometry='HollowCones', AddStatic=True, \
33              VelocityField='AccPlaw', Disk=True)
34 model = OL.Nebular([4958.911, 5006.843], **kwargs)
35 # update some parameters
36 model.update_params(['TerminalVelocity'], [500, 30, 15, 45])
37 model.update_params(['OpeningAngle', 'CavityAngle', \
38                    'Inclination'], [60, 30, 60])
39 model.update_params(['FluxOutflow1', 'FluxStatic1'], \
40                    [1/2.98, 1/2.98]) # Storey & Zeppen 2000
41 # simple trust-reflective fit for initial guess
42 tr_kwargs = dict(p0=model.get_params(), \
43                 bounds=model.get_bounds(), sigma=flux_error)
44 p0, c0 = curve_fit(model.Profile, wave, flux, **tr_kwargs)
45 model.update_params(model.get_param_names(), p0)
46 # initialize walkers and sampler and run the sampler
47 init, nwalk = model.init_params()
48 # use the custom prior and likelihood
49 model.log_prior = MethodType(log_prior, model)
50 model.log_likelihood = MethodType(log_likelihood, model)
51 # run the MCMC sampler
52 sampler = emcee.EnsembleSampler(nwalk, model.npar, \
53                               model.log_probability, args=(wave, flux, flux_error))
54 sampler.run_mcmc(init, 1200, progress=True)
55 samples = sampler.get_chain(discard=200, flat=True)
56 # extract parameters from posterior sample
57 for i, param in enumerate(model.get_param_names()):
58     value = nanquantile(samples[:, i], 0.5)
59     model.update_params(param, value)
60 # print line profile parameters to terminal
61 model.print_params()
62 # obtain outflow properties
63 props = OL.Properties(model)
64 # print outflow properties to terminal
65 props.print_props()

```

APPENDIX E: POSTERIOR SAMPLING

All posterior samples for each of the OutLines modeling cases were obtained using emcee (Foreman-Mackey et al. 2013) and visualized with figures produced by corner (Foreman-Mackey 2016) and subsequently adapted. Results are shown for NGC 5471 Knot A in Figure E1, the super star cluster of Green Pea J1044+0353 in Figure E2, Mrk 1486 in E3, and the Seyfert 2 nucleus of NGC 2992 in E4.

This paper has been typeset from a $\text{\TeX}/\text{\LaTeX}$ file prepared by the author.

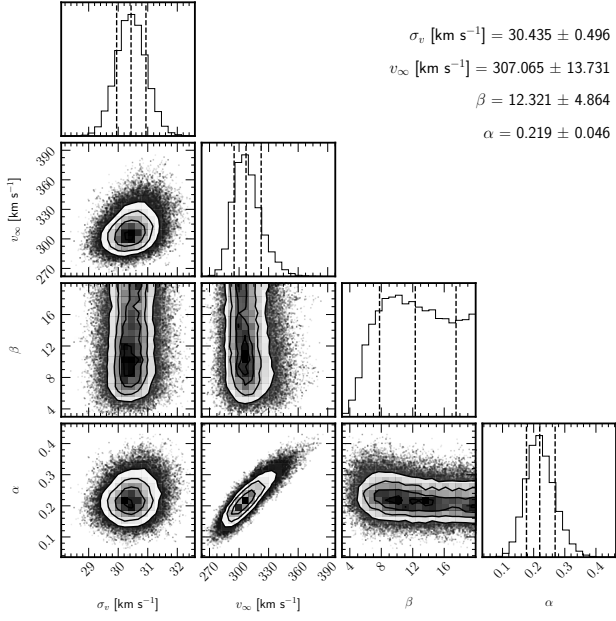


Figure E1. Posterior sampling of OutLines line profile parameters for [S II] λ 6716, 6731 in giant extragalactic H II region NGC 5471 Knot A. The parameters are CAK theory velocity field β , terminal velocity v_∞ , and power law density profile α .

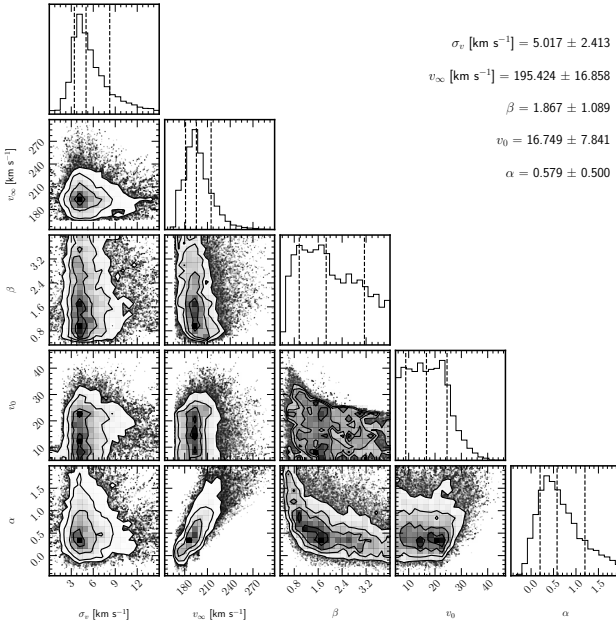


Figure E2. Posterior sampling of OutLines line profile parameters for C II λ 1334 in the super star cluster of Green Pea J1044+0353. The parameters are CAK theory velocity field β , terminal velocity v_∞ , and power law density profile α .

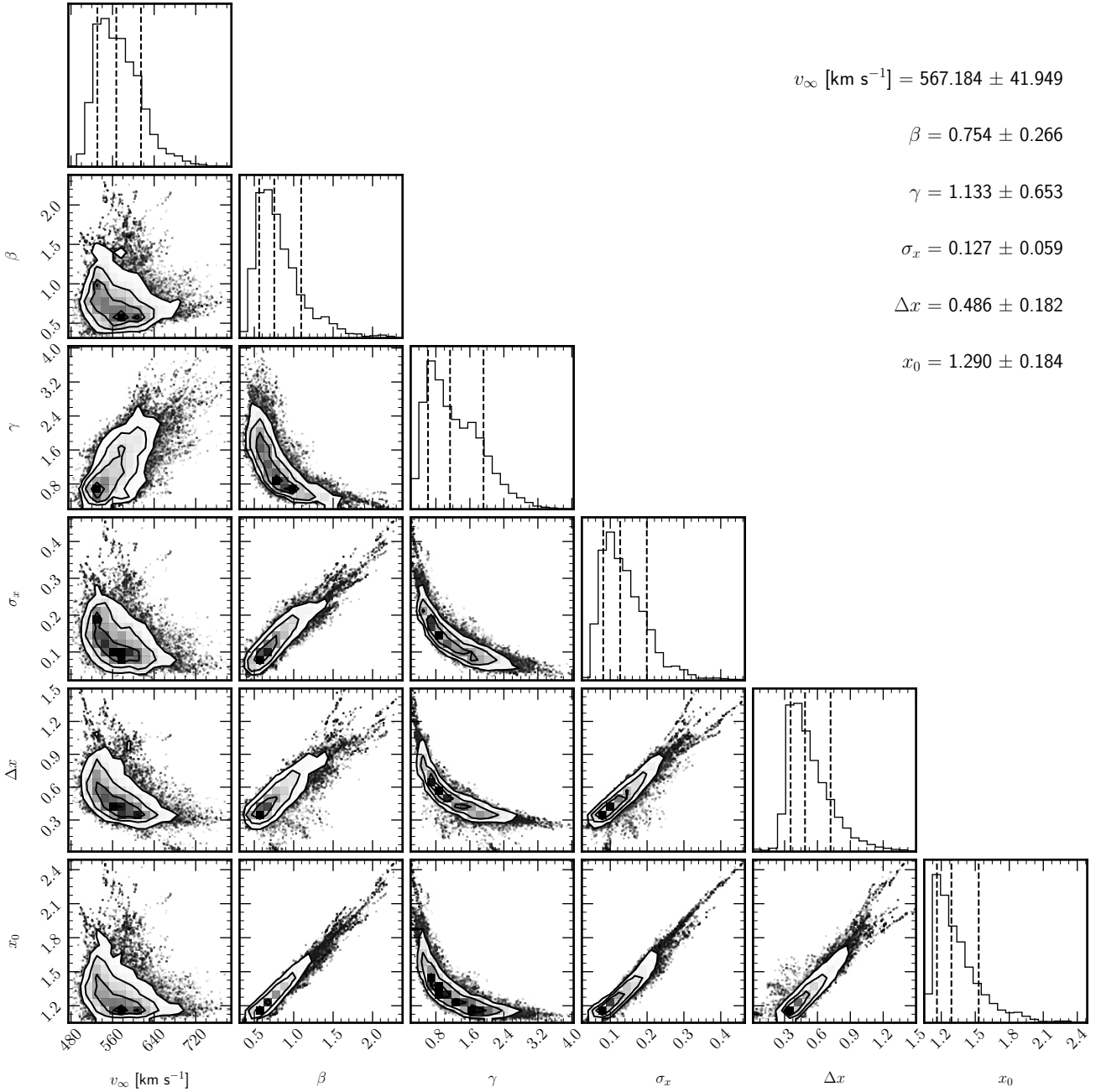


Figure E3. Posterior sampling of OutLines line profile parameters for Si II $\lambda 1190, 1193$ in starburst galaxy Mrk 1486. The parameters are CAK theory velocity field β , terminal velocity v_{∞} , and damped pulses with minimum radius x_1 , shell thickness σ_x , and interval distribution x_k . α .

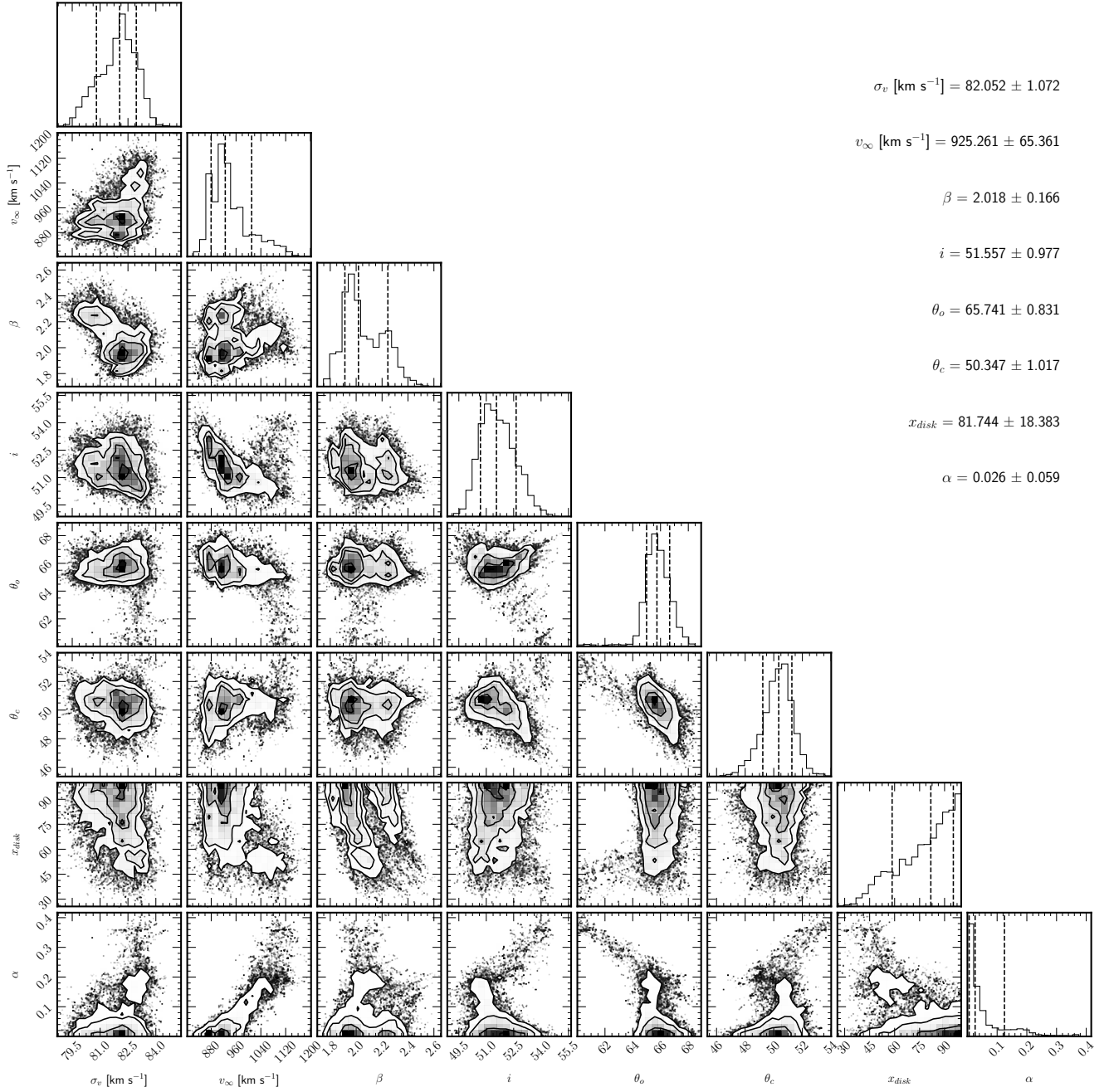


Figure E4. Posterior sampling of OutLines line profile parameters for [O III] λ 4959, 5007 in the Seyfert 2 nucleus of NGC 2992. The parameters are acceleration power law velocity field β , terminal velocity v_∞ , power law density profile α , and the hollow cone plus disk geometry components of inclination i , opening angle θ_o , cavity angle θ_c , and disk radius x_d .